Mach Effects for in Space Propulsion: Interstellar Mission

NIAC Case Study: Award NX17AJ78G

Written by PI Heidi Fearn, together with
Co Institutional-PI (Program Manager) Gary C Hudson
Co-PIs Thomas Marshall Eubanks, Bruce Long, José Rodal,
Consultants Paul March, James F. Woodward &
Graduate Student Nolan van Rossum.

Mission Statement: *To explore the feasibility of building a Mach Effect propulsion system capable of reaching Proxima Centauri, with a close encounter of Proxima b, in significantly less than a human lifetime (20-25 yrs.) and to conceptualize an interstellar probe using the Mach Effect propulsion method. To gather data and send back to Earth, within the 25 year mission duration.*

Table of Contents …….. 1

Dedication …… 2

Summary Chart …… 3

1. Introduction ……..…… 4

2. Basic Theory of the MEGA drive…….…… 6

3. Simple Model with force prediction……..…….…….. 9

4. Recent Experimental Results ……18

5. Analytical solution of the partial differential equations …….. 28

6. Preliminary mission suggested to the solar gravity lens……..…… 39

7. Probe design & shielding……..……... 41

7.1 Design of Probe ……..… 41

7.2 Communications with Earth on probe ……..… 43

7.3 Navigation system on probe ……. 46

7.4 Power Plant onboard (fission or fusion?)……. 46

8. S.W.A.P. analysis (Size, Weight & Power)……..….. 49

9. S.W.O.T analysis (Strength, Weaknesses, Opportunities and Threats)…… 50

10. Conclusions & Recommendations…….…... 50

11. References …… 51

Appendix A: Circuit upgrades feedback/control…… A1-A5

Appendix B: Q & A NIAC Symposium ……..…….. B1-B6

This study is dedicated to the memory of our friend and colleague Bruce Long.

Mach Effects for In Space Propulsion Interstellar Mission

H. Fearn CSUF Physics & Space Studies Institute

What is it?

Mach Effect Gravity Assist (MEGA) drive. A propellant-less propulsion device. Consistent with General Relativity, no new physics. Electrical energy in, unidirectional reaction out. TRL1, lab demonstrated but short duration.

How can it be used?

MEGA drive can potentially replace any in-space propulsion system, from reaction/attitude control to primary spacecraft propulsion.

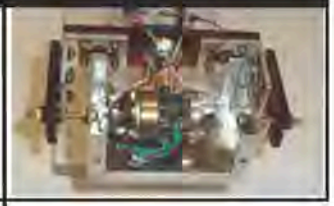

Study Approach

1. Improvement of current laboratory-scale devices to provide long duration thrusts for practical propulsion. (Chirped pulsed AC.)
2. Design and develop power supply & electrical systems to provide feedback and control of the input AC voltage and frequency, to improve efficiency of MEGA drive.
3. Using best theoretical model from tasks 1 & 2, design the propulsion system required to send 400 Kg of payload to Proxima Centauri with a mission duration (one way) of 20 years, including a rendezvous with Proxima Centauri b.

Benefits
If Concept Eventually Succeeds:

• Scalable electrically- powered solid-state propulsion w/o exhaust

• Potentially *spectacular* fast transit times for solar system and beyond.

Of this Study Now:

Moderately near-term in-space propellant-less propulsion for small to medium spacecraft.

Other considerations: Offers potential path to revolutionary interstellar propulsion

Evaluation Notes

1. Introduction

Our mission is to deliver a probe with 400Kg of payload to Proxima b and send data back to Earth within a 25 year time frame. The probe design is set 20-25 years into the future with Mach Effect Gravity Assist (MEGA) drives and fission (fusion) reactors we do not presently possess (in 2017-8) but which could conceivably be available in the near future (20-25 years time frame) and be tested and in common use within 25 years. The great challenge is to traverse 4.2 light years, of a hazardous space environment, at sub light speeds, reaching a maximum speed of approximately 0.4c at the half waypoint. Fortunately, the MEGA drive does not suffer from the restrictions of the rocket equation and the only speed limit we see at this time is the velocity of light in a vacuum, c. The MEGA drive does not eject propellant, it only requires electricity to function and therefore no massive propellant tanks are required for the journey. See section 2 for a full description of the MEGA drive and how it works. We have the potential for all-axis attitude control and the ability to brake into the target system with the opportunity for multiple year exploration not afforded to a fly-by mission.

The electricity would be supplied by a fission (or fusion) reactor of approximately 5 MW-thermal and 1.5 MW-electric power. It has been suggested that these types of reactors will be available in 20-25 years time [1-3].

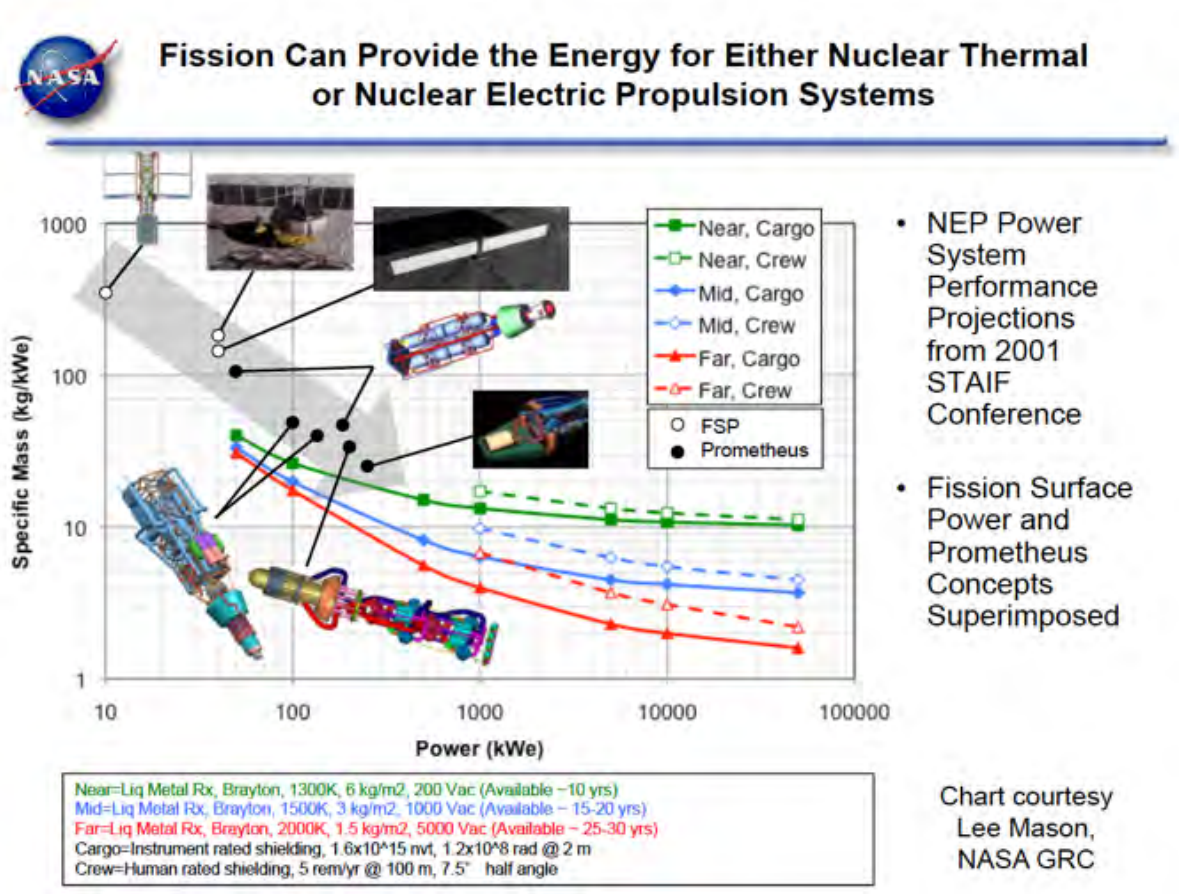

Figure 1.1 Projected availability of Fission reactions for the next 30 years. Chart courtesy of Lee Mason, NASA Glen Research Center [1].

The plan is to accelerate for 10 years then decelerate for a comparable time into the Proxima system. The incoming probe would decelerate sufficiently at a distance 50 – 100 Astronomical units from Proxima, and use an optical long range reconnaissance imager similar to the Lorri telescope on the New Horizons spacecraft (Pluto mission). This reconnaissance phase would be necessary to both validate the orbital ephemeris, search for other planets in the Proxima system, and to search for rings and other possible hazards to the spacecraft. Then after the reconnaissance phase, the spacecraft would proceed to go into orbit around Proxima b and take data. Even with a laser communications system and a 1 meter optical telescopes for communications, data return would take several years at a rate of 3 Gigabytes / year (1.5 kbps with a 50% duty cycle) In order to accelerate to the half way point in 10 years we require a constant acceleration of 0.4 m/s^2. Figure 1.2 shows an artist's impression of the probe design, which is driven by the requirements of thermal control (requiring an extensive radiator array) and shielding from both the reactor and the Interstellar Medium (ISM), which acts as a directed radiation beam at relativistic velocities. The engineering tradeoffs that went into this design are described further in Section 6.

In order to accelerate to the ½ way point in 10 years we require and acceleration of 0.4 m/s^2. This acceleration (a) can be simply calculated as follows;
A distance of 2.1 Ly =s = 2.1 x 365x24 x3600 x3 x 10^8 m = 1.98676x10^{16}m. The 10 year time in seconds is t= 10x365x24x3600 = 3.1536x10^8 sec. Hence starting from rest the acceleration a required is a = $2s/t^2$= 0.4 m/s^2. At the half waypoint the maximum velocity (v) attained will be v = a t = 0.42 c.

Mission Variant 1 - A 20 year journey that stops at Proxima b.

Spaceship acceleration = 0.38937 m / sec^2 (that is before adding the Sun's and Proxima's acceleration).

Spacecraft thrust reversed at 3715.0 days = 10.1711 years at 2.1214192 lyr from Proxima. V = 125017.90 km/sec = 0.41701 c

End of Mission is at;

Duration = 7304.728 days = 19.9993 years, Distance from Sun = 268304.91 AU = 4.2425734 lyr from Proxima = 0.05 AU = 0.0000008 lyr, V = 4320.11 km/sec = 0.01441 c

10 days out: Distance to Proxima = 27.94 AU = 0.0004418 lyr, V = 4680.90 km/sec

100 days out: Distance to Proxima = 349.94 AU = 0.0055334 lyr, V = 7708.67 km/sec = 0.02571 c

---

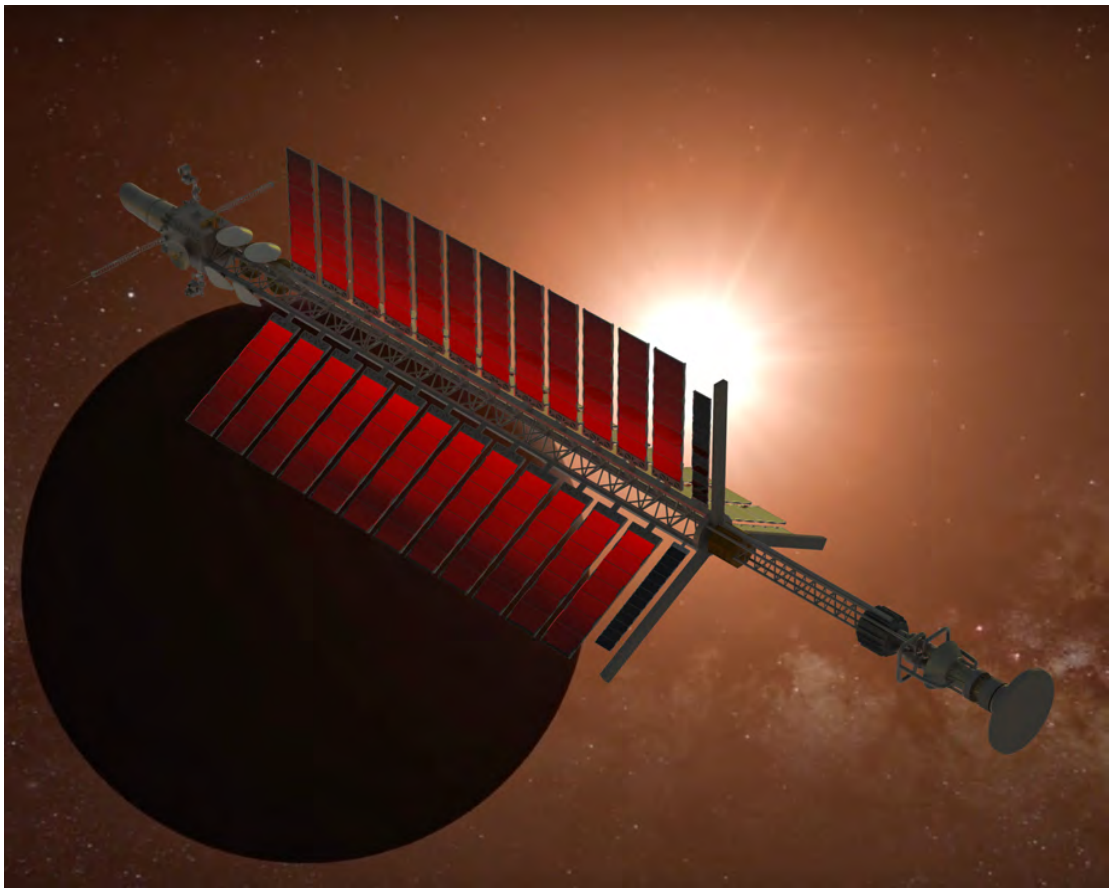

Figure 1.2 An artist's impression of the new probe design. The SSI-Lambda is seen in front of Proxima B with Proxima Centauri in the background.

2. Basic theory of the MEGA drive

Summarized from Estes Park Advanced Propulsion workshop 2016. [4]
Mach effects are fluctuations in the rest masses of extended objects as they are accelerated by external forces. This is a consequence of the action of the total (local and cosmic) gravitational field acting as the inertial reaction force that resists the acceleration, excited by the action of the accelerating external force. The predicted phenomena in question, in the relativistic Newtonian limit, arise from considering the effect of an "external" accelerating force on a massive, extended test particle. Instead of assuming that such an acceleration will lead to the launching of a (ridiculously minuscule) gravitational wave and asking about the propagation of that wave, one assumes that the inertial reaction force, acting through the accelerating test particle, experienced by the accelerating agent is caused by the action of, in Dennis Sciama's words, "the radiation field of the universe". Then, allowing that the inertial force is produced by the gravitational action of chiefly distant matter, one asks, given the field strength as the inertial reaction force per unit mass, what is the local source charge density at the test particle? Taking the direction of the accelerating force to be positive, the field strength at the test particle is just minus the derivative of the four momentum of the test particle with respect to proper time divided by the mass of the test particle.

We call attention here to an issue that can be the source of confusion. The time-like part of the four momentum is $mc = \gamma m_0 c$, where m_0 is the rest mass of the test particle. One sometimes hears

it claimed that rest mass is a constant. This statement, as a general assertion, is simply false. It may be true for structure less elementary particles. But for systems as simple as colliding billiard balls, it is obviously wrong during the collision. This means that when the derivative of $\gamma m_0 c$ is taken, terms involving the derivative of m_0 cannot be set equal to zero. Life can be a lot more complicated when rest mass isn't treated as a constant. But that's our reality.

The answer to the local sources question is obtained by taking the four-divergence of the field strength at the test particle. The field equation that results from these operations is:

$$\nabla^2\phi - \frac{1}{\rho_0 c^2}\frac{\partial^2 E_0}{\partial t^2} + \left(\frac{1}{\rho_0 c^2}\right)^2\left(\frac{\partial E_0}{\partial t}\right)^2 = 4\pi G\rho_0 \quad . \tag{1}$$

In this equation ϕ is the scalar potential of the gravitational field, ρ_0 the local proper matter density, E_0 the local proper energy density, c the vacuum speed of light, and G Newton's constant of gravitation. This equation looks very much like a wave equation. However, the space-like part (the Laplacian) involves a scalar potential, whereas the time-like part (the time-derivatives) involves the rest energy density. (The complete derivation of these effects can be found in Chapter 3 of *Making Starships and Stargates*, [5].) Were we dealing with any other interaction than gravity and inertia, we would be stuck at this point, for there would be no way to extract a time-like term from the rest energy dependent terms to complete and isolate the d'Alembertian of ϕ on the left hand side of Equation (1).

But we are not dealing with any old (or new) field. We are dealing with gravity understood, as Einstein did, to encompass inertia. When inertial forces arise from the gravitational action of chiefly distant matter, one finds that the total gravitational potential everywhere/when must be locally measured to be equal to the square of the speed of light.[1] And you don't even have to fudge to get the dimensions to turn out right. The dimension of ϕ is velocity squared. If ϕ isn't equal to the square of the speed of light, then inertial forces are not equal and opposite to applied forces. That is, Newton's third law is violated.

Now, Equation (1) can be put into the form of a standard classical wave equation by using the gravitational origin of inertia to "separate variables", for the gravitational origin of inertia implies more than the statement above involving the origin of inertial reaction forces. Indeed, it actually implies that the origin of mass is the gravitational interaction. In particular, the inertial masses of material objects are a consequence of their potential energy that arises from their gravitational interaction with the rest of the matter in the causally connected part of the universe. That is, in terms of densities,

$$E_g = \rho\phi \quad , \tag{2}$$

where E_g is the local gravitational potential energy density, ρ the local "quantity of matter" density, and ϕ the total gravitational potential at that point. (Note that it follows from Sciama's

[1] This is exactly true in the vector approximation to general relativity. When the calculation of inertial forces is done in the second rank tensor version of general relativity, a factor of 4 appears that complicates things a bit.

analysis that $\phi \equiv c^2$, so Equation (2) is nothing more than the well-known relationship between mass and energy that follows from special relativity theory if E_g is taken to be the total local energy density.) Using this form of the gravitational origin of inertia, we can write:

$$E_0 = \rho_0 \phi , \tag{3}$$

and this expression can be used in Equation (1) to affect the separation of variables. After some straight-forward algebra (recounted in *making Starships and Stargates*) we find that:

$$\nabla^2 \phi - \frac{1}{c^2}\frac{\partial^2 \phi}{\partial t^2} = 4\pi G\rho_0 + \frac{\phi}{\rho_0 c^2}\frac{\partial^2 \rho_0}{\partial t^2} - \left(\frac{\phi}{\rho_0 c^2}\right)^2\left(\frac{\partial \rho_0}{\partial t}\right)^2 - \frac{1}{c^4}\left(\frac{\partial \phi}{\partial t}\right)^2 , \tag{4}$$

or, equivalently,

$$\nabla^2 \phi - \frac{1}{c^2}\frac{\partial^2 \phi}{\partial t^2} = 4\pi G\rho_0 + \frac{\phi}{\rho_0 c^4}\frac{\partial^2 E_0}{\partial t^2} - \left(\frac{\phi}{\rho_0 c^4}\right)^2\left(\frac{\partial E_0}{\partial t}\right)^2 - \frac{1}{c^4}\left(\frac{\partial \phi}{\partial t}\right)^2 . \tag{5}$$

This is a classical wave equation for the gravitational potential ϕ, and notwithstanding the special circumstances invoked in its creation, it is general and correct, for when all the time derivatives are set equal to zero, Poisson's equation for the potential results. That is, we get back Newton's law of gravity in differential form. You might think that general relativity is not involved in this calculation since we are working in the Newtonian approximation with flat spacetime. That would be a serious mistake. This calculation only works because inertial effects are gravitational, giving us Equation (3) to use to separate variables. Curvature, by itself, is not the essential core of general relativity theory.

The transient source terms on the right hand sides of Equations (4) and (5) that are those of interest to us, for if they encode real phenomena, a real prospect that we will eventually be able to get out of our gravity wells (terrestrial and solar) exists.

In the case of Mach effect rest mass fluctuations we assume that Einstein really understood his own theory of general relativity. That he was right about inertia being a gravitational effect built into his theory. That assumption is what dictates that $\phi = c^2$ and $E_o = \rho_o c^2$, the conditions that must be true for the calculation of rest mass fluctuations to be true. Should you think that "matter" (stuff that gravitates) at cosmic distances should have no effects locally, this may seem miraculous. But common sense suggests otherwise, for as the gravitational influence of matter at a distance R decreases with the inverse square of R (in the Newtonian approximation), the amount of stuff in a spherical shell (of thickness dR) at distance R increases with the square of R. So, generally, distant stuff is, gravitationally speaking, just as important as local stuff. And there is an utterly gigantic amount of distant stuff out there.

To transform the predicted rest mass fluctuations in the source terms of Equations (4) and (5) we note that they can be written:

$$\delta\rho_0(t) \approx \frac{1}{4\pi G}\left[\frac{\phi}{\rho_0 c^4}\frac{\partial^2 E_o}{\partial t^2} - \left(\frac{\phi}{\rho_0 c^4}\right)^2\left(\frac{\partial E_0}{\partial t}\right)^2\right], \quad (6)$$

or, taking account of the fact that $\phi/c^2 = 1$,

$$\delta\rho_0(t) \approx \frac{1}{4\pi G}\left[\frac{1}{\rho_0 c^2}\frac{\partial^2 E_o}{\partial t^2} - \left(\frac{1}{\rho_0 c^2}\right)^2\left(\frac{\partial E_0}{\partial t}\right)^2\right], \quad (7)$$

where the last term in Equations (4) and (5) has been dropped as it is always minuscule. It is in the transient proper matter density effects – the RHSs of Equations (6) and (7) – that we seek evidence to demonstrate that the origin of inertia, as conjectured by Mach, Einstein, Sciama, and others, is in fact the gravitational interaction between all of the causally connected parts of the universe.

The obvious way to test for the presence of proper matter density fluctuations of the sort predicted in Equations (6) and (7) is to subject capacitors to large, rapid voltage fluctuations. Since capacitors store energy in dielectric core lattice stresses as they are polarized, the condition that E_0 vary in time is met as the ions in the lattice are accelerated by the changing external electric field. If the amplitude of the proper energy density variation and its first and second time derivatives are large enough, a detectable mass fluctuation should ensue. That mass fluctuation, δm_0, is just the integral of $\delta\rho_0(t)$ over the volume of the capacitor, and the corresponding integral of the time derivatives of E_0, since $\partial E_0/\partial t$ is the proper power density, will be:

$$\delta m_0 = \frac{1}{4\pi G}\left[\frac{1}{\rho_0 c^2}\frac{\partial P}{\partial t} - \left(\frac{1}{\rho_0 c^2}\right)^2\frac{P^2}{V}\right], \quad (8)$$

where P is the instantaneous power delivered to the capacitor and V the volume of the dielectric. *Note that the assumption that all of the power delivered to the capacitors ends up as a* proper *energy density fluctuation is an optimistic.* Nonetheless, it is arguably a reasonable place to start. A more recent theoretical treatment is available using scalar-tensor gravitational theory [x].

A natural question to ask now is: How does a δm_0 led to a motion of the device? We answer this question in the next section using a simplified model of the MEGA drive.

3. Simple Model with force prediction

What follows is a description of the MEGA drive component parts. At the core is a stack of lead-zirconate-titanate (PZT) 19 mm diameter by 2 mm thick plates. Silver electrodes are deposited on the flat surfaces of the plates. PZT is a ferroelectric material with a dielectric constant typically of more than 1000 that, because of the asymmetry of the crystalline structure of the material, can be polarized by the application of electric fields. If mechanical stresses are applied to polarized PZT,

generally, an electric field is induced in the material and electric charge appears on the surfaces of the material. The inverse of this process is to apply an electric field to the material (by charging adjacent electrodes) and produce a mechanical deformation of the material. The resulting piezoelectric strain is a linear function of the applied electric field. ``Poled'' PZT has many electromechanical applications, audio transducers and micro-linear actuators being typical uses.

The MEGA drive has a PZT stack made of 8 plates. Four pairs of plates, typically about 17 mm long when the electrodes and a strain gauge are included. The strain gauge consists of 2 unpowered PZT discs, which are only 0.3 mm thick. The piezoelectric stack is compressed by two end masses; an aluminum mass of 28.2mm diameter and about 4 mm thick and a cylindrical brass mass of the same diameter and 16mm long (or 19mm). Both masses are machined flat with a circular indent for the PZT stack, which is about 0.25mm deep. This indent is just enough to help align the stack while the device is put together, which is its sole purpose. The brass mass is at the supported end and is attached to the aluminum mass by six 2-56 stainless steel socket head cap screws (torqued to 4.0 in-lbf) as shown in Fig. 3.1. These screws have heat shrink tubing around them, for electrical insulation.

There is a thin rubber pad between the brass mass and the mounting bracket. The purpose of this padding, cut away so that it only surrounds the mounting 4-40 cap screws, is to minimize transmission of high frequency oscillations of the brass to the mounting bracket. The device is placed inside a sealed Faraday cage, which is mounted on the end of a balance beam able to twist in the horizontal direction. The deflection of the beam is measured with a Philtec optical sensor. The stack is subjected to ~200 Volts (amplitude) using 30-40 kHz frequency sine waves. The PZT is also electrostrictive, which produces a force due to the volumetric expansion of the stack at twice the frequency of the applied sine wave – that is, at the frequency of the mass fluctuation produced by the piezoelectric response- that combined with the mass fluctuation produces a net time-averaged force on the device.

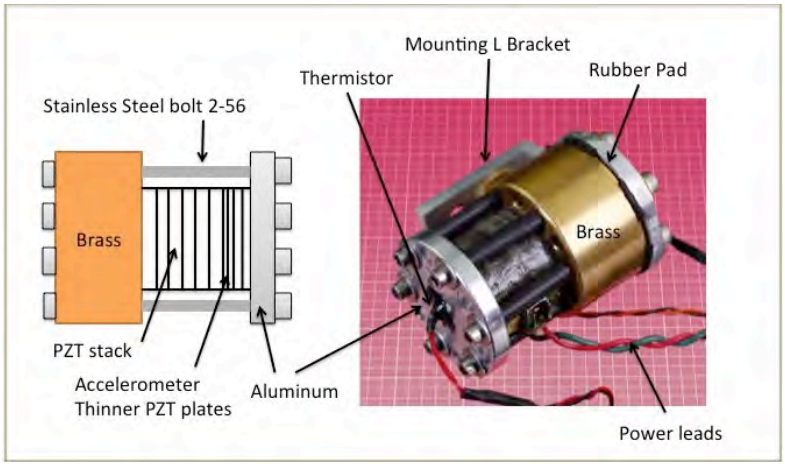

Figure 3.1. A MEGA device photograph. Taken by Charles Platt. The 6 Bolts have heat shrink wrapped around them to prevent electrical shorts.

The MEGA drives operates by producing a small fluctuation in the PZT mass, which is

undergoing energy fluctuations. This is used to produce a steady thrust, which we measure during the experiment. We push on the PZT (whose mass is fluctuating) when it is more massive and pull back when it is less massive, this produces a steady linear acceleration, which is detectable in the laboratory. (You can equally well think of this the other way; push when less massive, pull back when more massive for motion in the opposite direction.)

These devices can change direction with different input frequency, they do not need a rotation by 180 degrees. This steady force could be used to produce a propulsive force on a massive object without having to expel propellant from the object. This would be highly desirable from a space rocket point of view, which then would not have to carry a massive payload of expendable fuel. The mass fluctuation formula was derived by JFW many years ago and is in a recent book [5], it has also been re-derived for HF [4] using the advanced wave gravitational theory of Hoyle and Narlikar. Tests of Mach effect thrusters (or as they have recently been renamed, MEGA drives) in three labs other than ours, have produced thrust signatures like those we have obtained. These tests were performed by, Nembo Buldrini at FOTEC (Austria), George Hathaway in Toronto, and Martin Tajmar at Dresden Technical University. All these experiments have been conducted by experts, with very good facilities at their disposal. These results have been shared at a recent workshop in Estes Park, Colorado, in September 2016, [4]. This paper will show the latest experimental results and explain recent systematic testing, being performed in the laboratory, at CSU Fullerton, since January 2017.

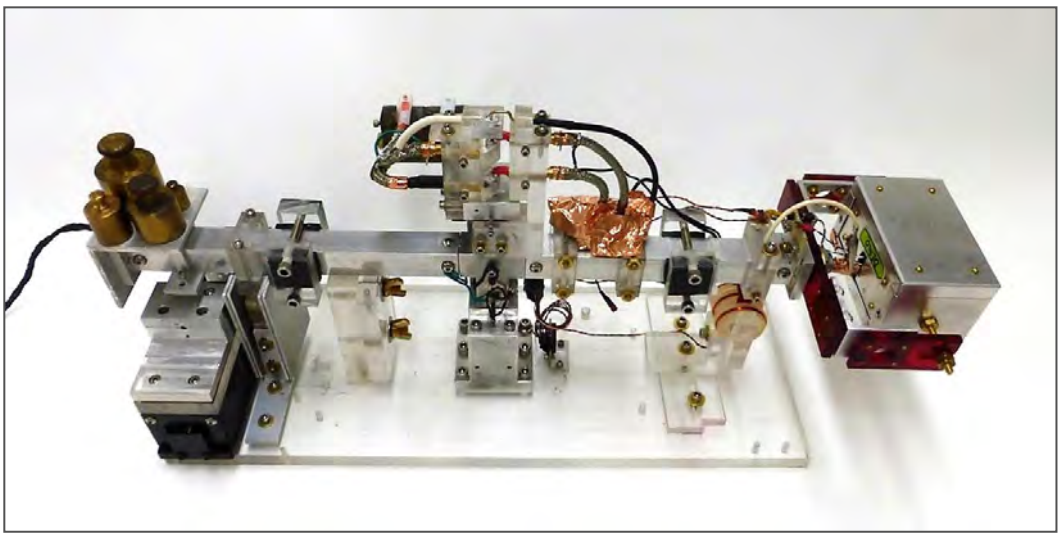

Figure 3.2. Torsion balance beam used at CSUF physics department. The Faraday cage is on the right. The coils below the cage are for calibration only and usually turned off. The brass masses on the top left are a counterweight for the Faraday cage. The Philtec optical sensor mount bracket and stepper motor are seen on the lower left. Just to the right of the black stepper motor is a magnetic damper. The power supply is fed into wires, threaded inside the rectangular aluminum beam arm, via galinstan contacts to prevent the weight of the power leads from torquing the beam to one side or the other when the power is applied. The galinstan contacts are centered above the C-flex flexural bearings of the balance beam. The device is mounted on the vertical side of the

Faraday cage, so it makes no difference whether the Faraday cage is oriented in one direction or inverted.

The torsional pendulum used at California State University Fullerton in shown in Figure 3.2. It is sensitive enough to measure 0.05μN of force.

Basic Theory of the MEGA drive operation

The basic theory for the MEGA drive has been given by JFW in many papers and in a recent book [5]. The idea is that Mach's principle as stated by Wheeler in [6,7] and in [8] is correct, inertia here is due to mass-energy from the distant matter in the universe. An extended body, undergoing acceleration (due to force1), with internal energy changes, can interact with the distant matter in the universe, instantaneously creating a mass fluctuation. This mass fluctuation can be used to generate thrust, if a second oscillating force is present, in sync with the oscillating mass. The center of mass (COM) of a system with oscillating mass can be shown to accelerate [9]. The calculation is very simple and can be reproduced here in a few lines.

Consider the mass spring arrangement in Figure 3.3 below. The masses m_1 and m_2 are coupled by a spring with spring constant k. The system of two masses and spring are free to move in space and not attached to anything. We measure the distance of the two masses from a fixed wall at x=0. For example the distance of mass m_1 to the fixed wall is x_1. The un-extended (or relaxed) length of the spring is L. Using the two masses as constant, we can write down two equations as follows;

$$\begin{aligned} m_1\ddot{x}_1 &= -k(x_1 - x_2 - L) + F_{12} \\ m_2\ddot{x}_2 &= +k(x_1 - x_2 - L) + F_{21} \end{aligned} \tag{1}$$

adding these equations gives,

$$\begin{aligned} & m_1\ddot{x}_1 + m_2\ddot{x}_2 = -k(x_1 - x_2 - L) + F_{12} + k(x_1 - x_2 - L) + F_{21} \\ & F_{12} = -F_{21} \\ & \Rightarrow m_1\ddot{x}_1 + m_2\ddot{x}_2 = 0. \end{aligned} \tag{2}$$

The COM of this mass-spring arrangement is given by

$$x_{com} = \left(\frac{m_1 x_1 + m_2 x_2}{m_1 + m_2} \right). \tag{3}$$

The acceleration of the COM, for masses taken to be constant, is therefore

$$a_{com} = \ddot{x}_{com} = \left(\frac{m_1 \ddot{x}_1 + m_2 \ddot{x}_2}{m_1 + m_2} \right) = 0 \tag{4}$$

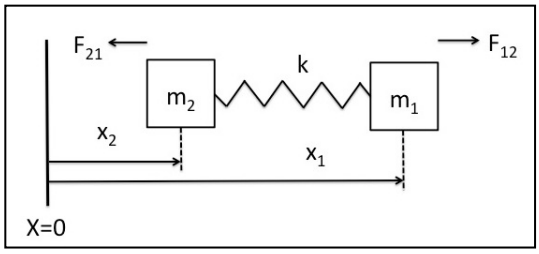

Figure 3.3 Simple two masses connected by a spring model.

However, if we allow the masses to change $dm_j/dt \neq 0$, where j=1,2,then starting from Eq. (3) and differentiating,

$$\begin{aligned} a_{com} = \ddot{x}_{com} = & \left(\frac{1}{m_1 + m_2} \right) \left[2\left(\dot{m}_1 \dot{x}_1 + \dot{m}_2 \dot{x}_2 \right) + \left(m_1 \ddot{x}_1 + m_2 \ddot{x}_2 \right) + \left(\ddot{m}_1 x_1 + \ddot{m}_2 x_2 \right) \right] \\ & - \left(\frac{2}{(m_1 + m_2)^2} \right) \left[\dot{m}_1 + \dot{m}_2 \right] \left[\left(m_1 \dot{x}_1 + m_2 \dot{x}_2 \right) + \left(\dot{m}_1 x_1 + \dot{m}_2 x_2 \right) \right] \\ & - \left(\frac{1}{(m_1 + m_2)^2} \right) \left[m_1 x_1 + m_2 x_2 \right] \left[\ddot{m}_1 + \ddot{m}_2 \right] + \left(\frac{2}{(m_1 + m_2)^3} \right) \left[m_1 x_1 + m_2 x_2 \right] \left[\dot{m}_1 + \dot{m}_2 \right]^2 \end{aligned} \tag{5}$$

Using $(m_1 \ddot{x}_1 + m_2 \ddot{x}_2) = 0$ from Eq. (2), the total mechanical momentum p is given by,

$$\begin{aligned} p &= m_1 \dot{x}_1 + m_2 \dot{x}_2 \\ \dot{p} &= \left(\dot{m}_1 \dot{x}_1 + \dot{m}_2 \dot{x}_2 \right) + \left(m_1 \ddot{x}_1 + m_2 \ddot{x}_2 \right) = \left(\dot{m}_1 \dot{x}_1 + \dot{m}_2 \dot{x}_2 \right) \end{aligned} \tag{6}$$

Momentum is not conserved, that is $\dot{p} \neq 0$, unless $\dot{m}_1 = -\dot{m}_2$. The unidirectional acceleration of the COM does not violate momentum conservation since momentum is not generally conserved (locally) in the case of oscillating masses. You need to consider the momentum of the entire universe, in order for the total momentum to be to conserved, which will indeed be the case. *This is a simple description only to give the reader the idea of where a COM motion can arise from changing masses.*

Let

$$u = x_1 - x_2 - L$$
$$\ddot{u} = \ddot{x}_1 - \ddot{x}_2 .$$

(7)

where L is the relaxed length of the spring. Subtracting the equations in Eq. (1) above gives,

$$\ddot{u} = \ddot{x}_1 - \ddot{x}_2 = -\frac{k}{m_1}(x_1 - x_2 - L) + \frac{F_{12}}{m_1} - \frac{k}{m_2}(x_1 - x_2 - L) - \frac{F_{21}}{m_2}$$
$$F = F_{12} = -F_{21}$$
$$\ddot{u} = -ku\left(\frac{1}{m_1} + \frac{1}{m_2}\right) + F\left(\frac{1}{m_1} + \frac{1}{m_2}\right)$$

(8)

Introducing the reduced mass μ,

$$\mu = \left(\frac{m_1 m_2}{m_1 + m_2}\right)$$
$$\frac{1}{\mu} = \left(\frac{1}{m_1} + \frac{1}{m_2}\right)$$

(9)

Thus from Eq. (8) we get,

$$\ddot{u} = -k\frac{u}{\mu} + \frac{F}{\mu}.$$

(10)

Using μ_0 in Eq. (9) for the rest masses m_{01} and m_{02}.

$$F = F_0 \cos(\omega t)$$
$$m_1(t) = m_{01} + \delta m_1 \cos(\omega t + \phi_1)$$
$$\dot{m}_1(t) = -\omega \delta m_1 \sin(\omega t + \phi_1)$$
$$\ddot{m}_1(t) = -\omega^2 \delta m_1 \cos(\omega t + \phi_1)$$

(11)

where masses m_{01} , m_{02} and phases ϕ_1, ϕ_2 are constant. The mass change δm is considered very small. Similar equations to Eq.(11) hold also for m_2 and its derivatives with respect to time. We take for the reduced mass $\mu = \mu_0$ (when the masses do not change) and $\omega=\omega_0 = (k/\mu_0)^{1/2}$. The solution for u(t) is found as follows:

$$u(t) = x_1(t) - x_2(t) - L = u_0 \cos(\omega t) = \mathrm{Re}[u_0 e^{i\omega t}]$$
$$\dot{u} = i\omega u$$
$$\ddot{u} = -\omega^2 u$$
$$(\omega_0^2 - \omega^2) u_0 = \frac{F_0}{\mu_0}$$

(12)

where the last equation above, comes from substituting the results for u(t) and its derivatives into Eq. (10) using constant masses. This gives us the expression for u_0. The time dependent u(t) solution can be written, taking F (as defined in Eq. (11)) instead of F_0 in the last expression of Eq.(12) above,

$$u(t) = \left(\frac{F_0}{\omega_0^2 - \omega^2} \right) \frac{\cos(\omega t)}{\mu_0} .$$

(13)

Now using,

$$\ddot{u} = \ddot{x}_1 - \ddot{x}_2$$
$$m_{01}\ddot{x}_1 + m_{02}\ddot{x}_2 = 0$$

(14)

we can write

$$x_1(t) = \left(\frac{m_{02}}{m_{01} + m_{02}} \right) u(t)$$
$$x_2(t) = -\left(\frac{m_{01}}{m_{01} + m_{02}} \right) u(t)$$

(15)

substituting these expressions into the equation for the COM acceleration Eq.(5), or alternatively in Eq. (6) we find,

$$\dot{p} = \left(\frac{\omega^2 F_0}{\omega_0^2 - \omega^2} \right) \left[\frac{\delta m_1}{m_{01}} \sin(\omega t) \sin(\omega t + \phi_1) - \frac{\delta m_2}{m_{02}} \sin(\omega t) \sin(\omega t + \phi_2) \right]$$

$$\dot{p} = \frac{1}{2} \left(\frac{\omega^2 F_0}{\omega_0^2 - \omega^2} \right) \left[\frac{\delta m_1}{m_{01}} \cos\phi_1 - \frac{\delta m_2}{m_{02}} \cos\phi_2 \right] = (m_{01} + m_{02}) a_{com} \tag{16}$$

where terms in δm^2 have been dropped, as being negligible. It can be shown that the COM acceleration, which has no sine or cosine oscillations in it, can be written as

$$a_{com} = \frac{1}{2(m_{01} + m_{02})} \left(\frac{\omega^2 F_0}{\omega_0^2 - \omega^2} \right) \left[\frac{\delta m_1}{m_{01}} \cos\phi_1 - \frac{\delta m_2}{m_{02}} \cos\phi_2 \right] \tag{17}$$

which agrees with [9] except here we have a factor half. It appears that a steady linear acceleration of the COM, not just an oscillation, is possible when the masses are allowed to change and the masses are unequal. If the masses m_1 and m_2 were the same and changed in time by the same amount, there would be no linear COM acceleration possible. In reality we need to also consider damping.

For the detailed theory of the MEGA device, we refer the interested reader to [4,5] and papers therein. The mass fluctuation can be derived directly from the gravitational absorber theory of Hoyle and Narlikar [10]. This fully Machian theory does not require a steady state universe. Simply omit the creation C-field and it is an expansion theory. The mass fluctuation appears in the Hoyle Narlikar field equation as the trace of the energy momentum tensor, see Fearn in [4]. The trace of the energy stress tensor ($T=T_\lambda^\lambda$) comes into the derivation of the curvature by a slight modification of the field equations, shown in the gravitation text by Carroll [11] using a signature (+---) , or Weinberg [12],

$$R_{\mu\nu} = -\frac{8\pi G}{c^4} (T_{\mu\nu} - \frac{1}{2} T_\lambda^\lambda g_{\mu\nu}) ,$$

(18)

where we have put the speed of light c back into the expression. Here we shall merely state that the mass fluctuation expected in the device, given by a gravitational interaction with the distant matter in the universe, is δm_0 and is given by,

$$\delta m_0 = \frac{1}{4\pi G} \left[\frac{1}{\rho_0 c^2} \frac{\partial P}{\partial t} - \left(\frac{1}{\rho_0 c^2} \right)^2 \frac{P^2}{V} \right]$$

(19)

where P is the instantaneous power delivered to the capacitor, ρ_0 is the density of the PZT, c is the velocity of light and V the volume of the PZT stack dielectric. This is Eq. (8) of section 2. Note that the assumption that all of the power delivered to the capacitors ends up as a proper energy density fluctuation is an optimistic, indeed, perhaps wildly optimistic, assumption.

In a very simplified picture, one can imagine the brass end mass varying only slightly due to heating, and the PZT and thinner aluminum end mass (thought of as one mass) having most of the variation of mass. The mass fluctuations would be very different and the masses are also unequal. The mass of the 16mm length brass is ~ 77g, the 4mm length Aluminum end mass is ~7.3g and the PZT stack has a mass of 48.6g. So combined the PZT and aluminum would be only 48.6g. The change in the brass mass would be minimal almost zero. One can at least see in this toy model, how the device can have an acceleration (not just an oscillation) of the COM from Eq. (17). In general, a real system would need to include damping. This model has no damping, but it would be straight forward to include as a dashpot say between the two masses together with the spring, see [4].

It is possible now to give an order of magnitude estimation of the force from the device. We will take the force to be approximated by $F = \dot{m}\dot{x}$ from Eq. (6) , where the extension of the stack with six, 2-56 stainless steel bolts, is $\Delta x \sim 5\mu m$ and the resonant frequency of operation is ~36 kHz, so the period of oscillation is Δt ~2.75 x 10^{-5} seconds. So $\dot{x} = \Delta x / \Delta t = 0.18$ m/s. Using the first term in Eq. (18) the value of δm ~6.27 x 10^{-6} kg. Using Power, P = I V, current I = 0.5 A, V=200 volts, density PZT, $\rho = 7.9 \times 10^3$ kg/m^3 and $G = 6.674 \times 10^{-11}$ m^{3}kg^{-1}s^2. We find the force $F \approx 1.09 \mu N$. The order of magnitude of this force is correct.

The model of the device, as two unequal masses which can vary in time (coupled by a spring and dashpot), including detailed numerical calculations of the force produced, has been given in by José Rodal [4]. This model too was deemed to simplistic and has since been modified to a full differential equation of a viscous elastic material with damping and entropy.

For the probe it is essential to take into account special relativity, since the velocity of the probe will reach 0.42c and the relativistic gamma factor will be ~1.102. The lowest order terms in the rate of change of the center of momentum then look like this,

$$\dot{v}_{CM} = \frac{\frac{m_1 \dot{x}_1}{\sqrt{1 - x_1^2/c^2}} + \frac{m_2 \dot{x}_2}{\sqrt{1 - x_2^2/c^2}}}{\frac{m_1}{\sqrt{1 - x_1^2/c^2}} + \frac{m_2}{\sqrt{1 - x_2^2/c^2}}} \quad + \text{higher order terms}$$

where the relativistic mass has been used. For this illustrative purposes the following assumptions are made:

(1) no damping
(2) very weak gravitational field
(3) uniform gravitational field with respect to the dimensions of the drive
(4) small spin and spin rates

(5) small strain

The velocities of the masses are $\dot{x}_1$ and $\dot{x}_2$. Time differentiation is shown by an overdot.

4. Recent Experimental Results

Initially a new device is first tested on a vector network analyzer (VNA) to determine its natural resonance frequencies. As an example, in figure 4. is shown the result of running white noise at 5 volts through our demonstration device on the VNA (Stanford Research 780 model). This particular device showed a resonant frequency around 36 kHz, slightly higher than the lowest impedance dip on the plot which was at 32.384 kHz.

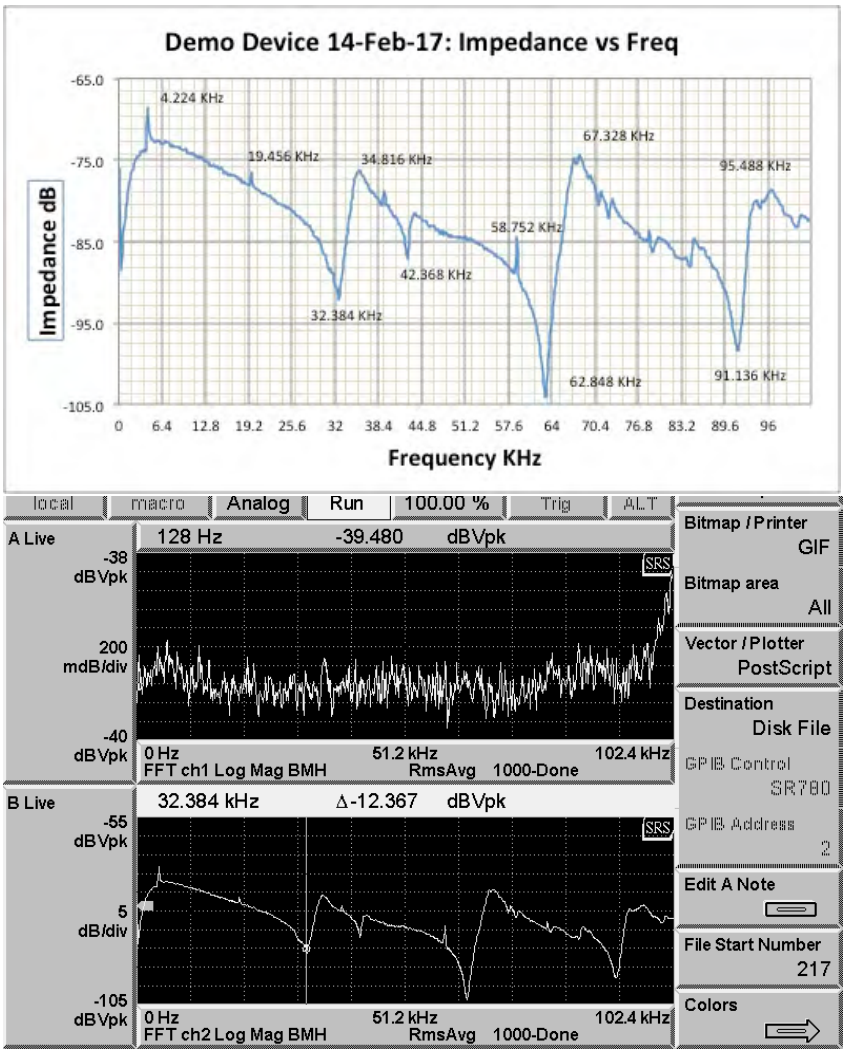

Figure 4.1 The upper diagram shows the frequencies of the Impedance dips and peaks. The lower picture is screenshot of the SR780 vector network analyzer screen. The upper window is the white noise, the lower window shows the impedance dips.

After measuring for the capacitance of the device and running it on the VNA the test device is placed into the Faraday cage. The whole balance beam is placed inside a vacuum chamber. The soft vacuum pressures we run at are around 5-10 mTorr. A typical run consists of taking ambient noise data for about 15 seconds, followed by a 3 second voltage pulse, on the resonant mechanical frequency of the device. This is followed by a frequency sweep (of about 10-30 kHz) through the resonant frequency for about 8 seconds and then a second on resonant pulse (for 3 seconds) and finally by more ambient noise for 15 or more seconds. The frequency sweep is a way of tracking the resonance frequency of the device. We find that when the device heats up the resonance frequency can change. We should see a large response to the voltage pulse at the resonant frequency (or very close to it). Since the sweep has the resonance at the center (and we usually sweep high to low frequency) if the large response occurs early (or late) in the sweep we can tell that the resonance has shifted higher (or lower) in frequency in relation to the center (resonance) frequency we were running at. For steady operation under optimal conditions, a resonance tracking circuit employing a feedback would be desirable.

We also routinely run the device in one orientation and then rotate the entire Faraday cage by 180 degrees and run the same experiment again. By rotating the Faraday cage, we have essentially reversed the direction of the device. Data is taken in one orientation and averaged, then we subtract off an average of runs done in the opposite direction, thereby eliminating any non-reversing thrust signatures. In effect, this eliminated any common mode noise. As an example, here is a single pulse averaged over a dozen runs given by two different groups. See figure 4.2. The data from Woodward was taken with a voltage of 200V amplitude. The data by Buldrini was taken using 200V peak-to-peak, so half the voltage Woodward was using. The force is known to vary (via experiment and theory) as voltage to the fourth power, which explains the discrepancy in the size of the forces seen. The force shown by Woodward is about 2μN which is ~13 times larger than Buldrini's result. However, double the voltage gives 2^4=16 times larger force. So that works out about right. Of course the devices used were not exactly identical.

The resonant AC voltage pulse at the resonant frequency gives a transient switch-on spike, then a steady force, then a switch-off spike in the opposite direction to the switch-on spike. See figure 4.3 and look back at figure 4.2 for comparison with experiment. Note that the switch off spike (in this particular orientation) adds to the steady force to give a larger force momentarily.

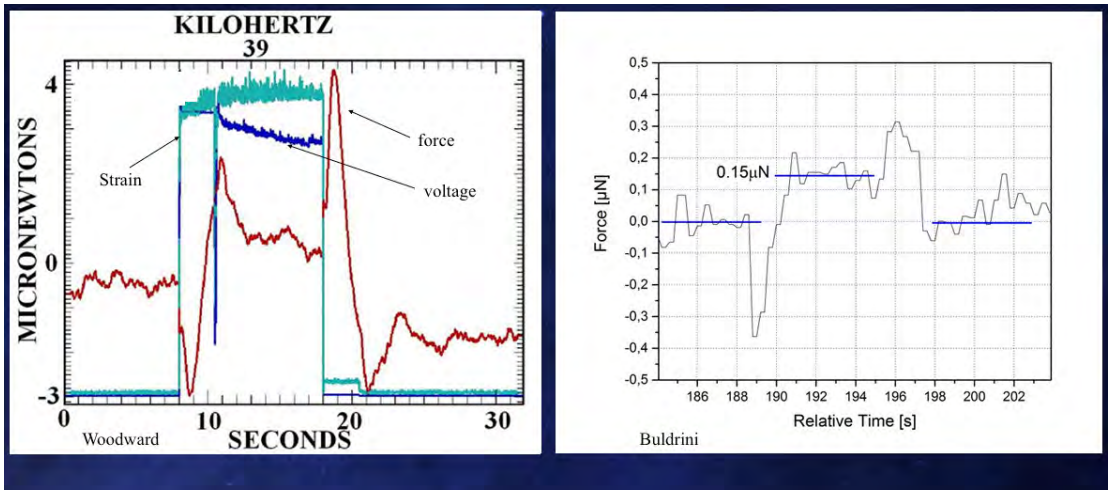

Figure 4.2 Test results by two groups Woodward (left) and Buldrini (right), showing a single on resonance pulse and data averaged over a dozen runs. Woodward was using twice the voltage (V) that Buldrini was

using. The force scales as V^4. For data on the left by Woodward, the jagged line is force, the darker (slightly lower) square pulse line is applied voltage (lasting 11 seconds) and the lighter square pulse is the strain gauge inside the stack. Photos taken from Buldrini [4].

It would be of interest to utilize the switch-off transient as a propulsive force and eliminate the switch-on transient, which is in the opposite direction. Then by using a rapid succession of these switch-off transients we might propel a craft along in space more efficiently than by using the steady thrust as he power duty cycle could be kept small.

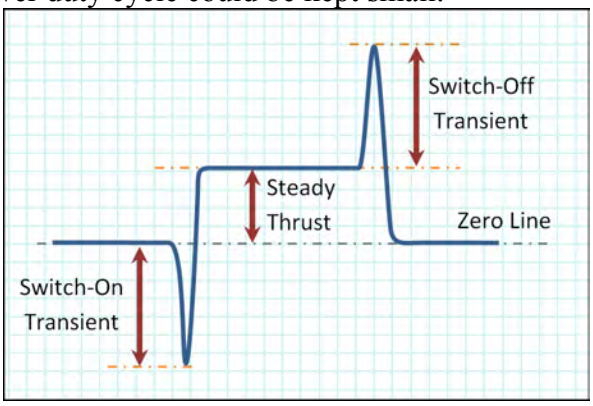

Figure 4.3 Diagram showing the main features of the force trace during the voltage pulse at the resonance frequency. Sometimes the horizontal dotted lines can be tilted, this is caused by thermal drift in the data. Diagram by Buldrini, [2].

Results

Since the force has been shown to go with the rate of change of power P, and dP/dt has opposite signs for the on and off transients, the thrust transients have opposite signs too. If the magnitudes of the thrust impulses are the same, or nearly the same, the off transient will cancel the on transient and the net thrust over one cycle will be small or zero. If everything were simple and linear, it might well be the case that the on and off impulses were equal and opposite. But the devices tested here are not simple and linear, so there is a real prospect that one of the transients can be suppressed, leaving the other transient unbalanced. The simplest way to accomplish this is to turn on or off either the on or off transient slowly, leaving the other transient prompt. Since these devices run on an electro-mechanical resonance of the device, there is a simple way to affect slow turn-on or turn-off. Say we want to turn the device on slowly (and off promptly). We simply energize the device with a voltage signal several kHz away from the resonant frequency. Then, using the control voltage of the voltage controlled oscillator, we bring the operating frequency onto resonance slowly. Code was written to affect this procedure. The result is shown in Figure 4.4. The quality of the thrust resolution is good enough to show an at first negative, and then positive going thrust as the frequency is brought down to resonance (by raising the oscillator control voltage). The switching transient that follows the power being switched off is obvious and cannot be due to power considerations as the power is off.

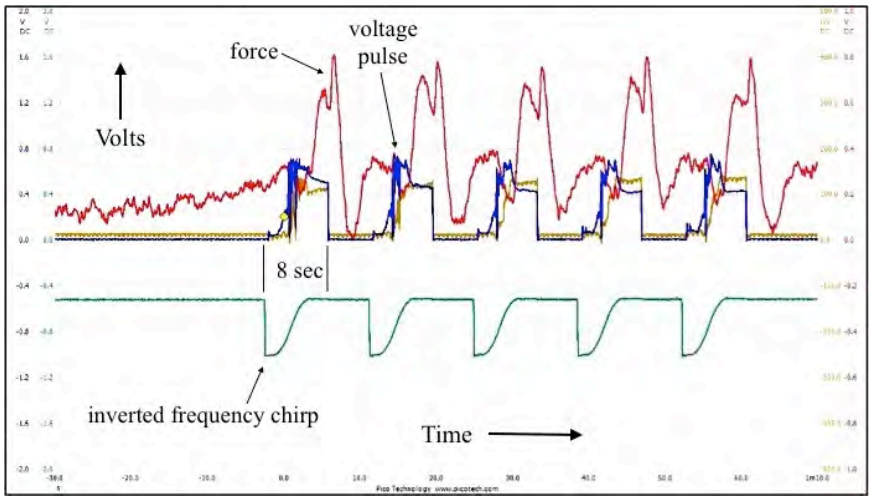

Figure 4.4 Chirped 8 second pulses. The pulses start at a frequency above the resonant frequency of the device and then slowly the pulse is tuned onto the resonant frequency. The lower line shows an inverted frequency change, the frequency actually starts high and gets tuned quadratically lower during the pulse. The square-like pulses represent the voltage amplitude applied to the device. The jagged line with the peaks in the force trace. This data was recorded using a Picoscope, model 4244.

When the Faraday cage is rotated by 180 degrees, the device is then forced in the opposite direction. The resulting force trace can be seen in figure 4.5.

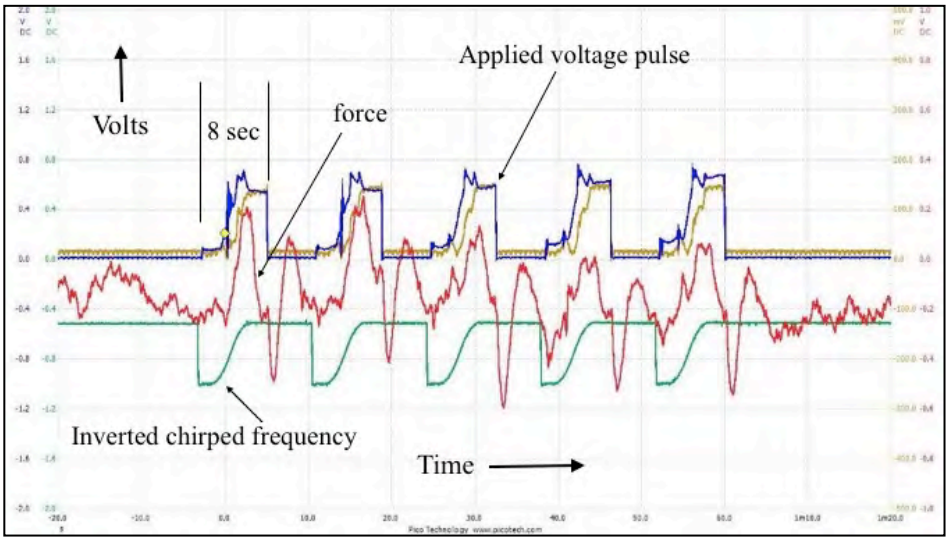

Figure 4.5 Chirped 8 second pulses. The pulses start at a frequency above the resonant frequency of the device and then slowly the pulse is tuned onto the resonant frequency. This jagged curve shows the force in the opposite direction as compared with figure 4.4. This force plot has a slight downward slope due to thermal drift. These plots are reproduced from the paper by JWF in the Estes Workshop [4].

It has also been observed that the direction of the force can change depending only on the frequency of the input voltage to the device. This was noticed, during a run of chirped pulses

where the frequency was changed inbetween pulses of the applied voltage. Figure 4.6. shows a set of chirped pulses which started off by using a slightly higher than resonance frequency, the voltage oscillator input frequency was set at 36.7 kHz. The sweep starts high then is swept down to the voltage oscillator input frequency. The actual resonance of the device was 36.3kHz, so between pulses the voltage oscillator frequency was lowered to 35.8 kHz so that the entire resonance is swept through. It appears that very close to the resonant frequency is another frequecy where the device would move in the opposite direction. It is reasonable to think that one could tune the device to move either in one direction or the opposite without having to rotate the device by 180 degrees. This would be a convenience for a space-drive, since it entails essentially no moving parts. (No gimbal required, as for ion drives and hence less weight.)

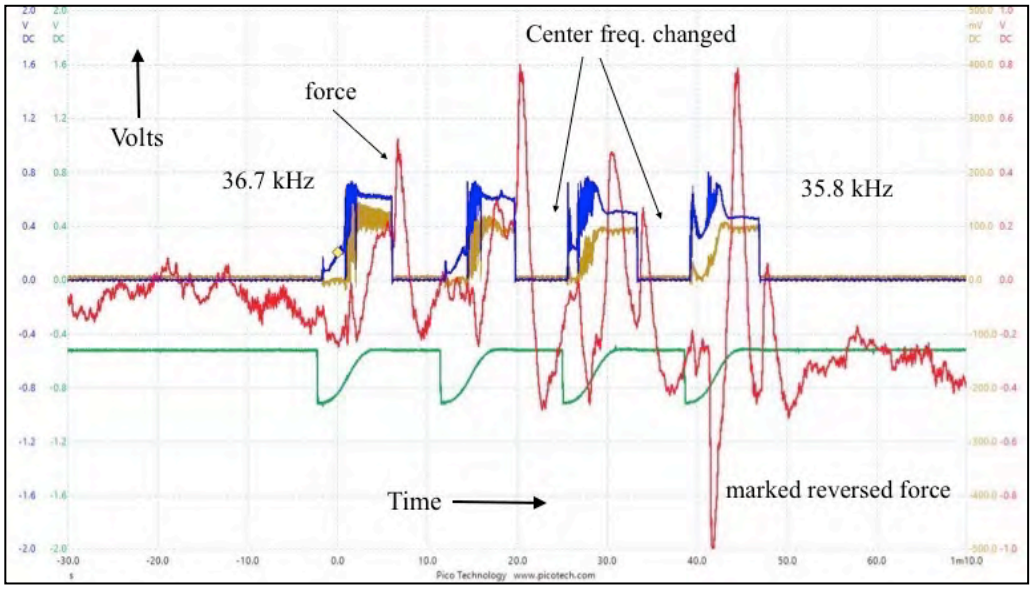

Figure 4.6 Force plot versus time showing a reversal in the direction due to frequency change.

Force dependence on Voltage

More recent chirp data (August 2017) has been used to compile a graph of force verses voltage. Excel was used to do a regression fit to the data points and a roughly V^4 dependence was shown. See Figure 4.7 below. Each black dot represents a chirp, most runs have 4 or 5 chirps in them. The different voltages are achieved by changing the settings on the amplifier. This work was first reported in [13,14].

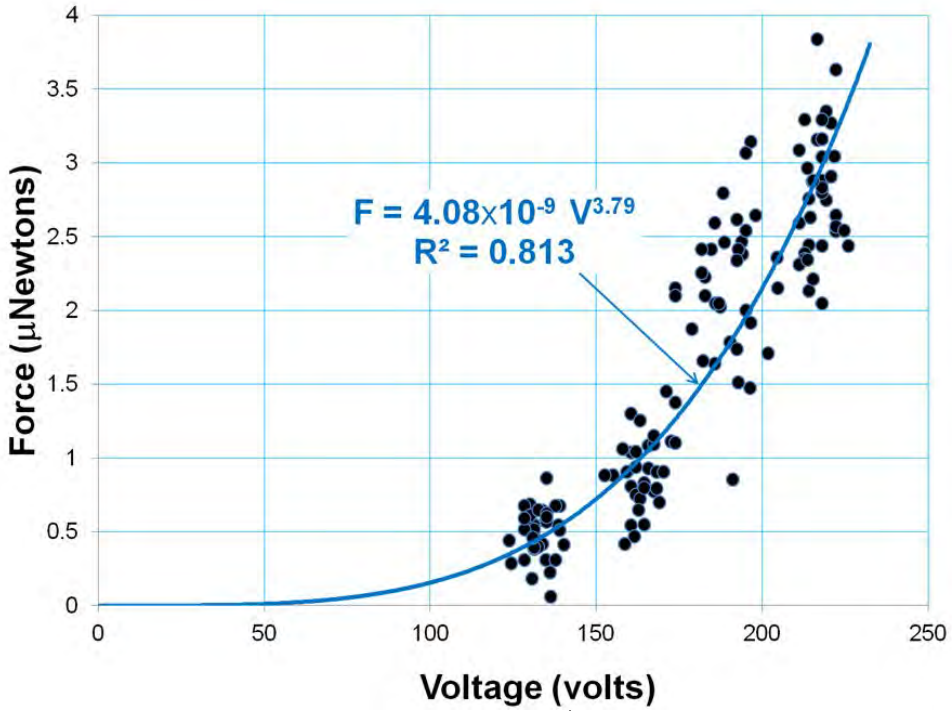

Figure 4.7 Force verses voltage plot showing a V^4 dependence.

Problems and Solutions

The PZT being used regularly at CSUF by JWF is purchased form Steiner Martins and is called SM-111 material. It has some nice properties which can be found online [15], on the steminc.com webpages. The material has reportedly a Young's modulus (stiffness) of $E=Y_{33}= 7.3 \times 10^{10}$ N/m^2, density of 7.6 g/cm^3 , the piezoelectric constant $d_{33}= 320 \times 10^{-12}$ m/V, a Curie temperature of 320 degree Celcius, a dissipation tan δ =0.4, and the mechanical quality factor, Q_m=1800. Well actually, we measured the Q_m and found it to be closer to 80 when the discs are glued together into a stack and Dr. Martin Tajmar also measured the Q at his facility in Dresden TU and found a $Q_m \sim$ 60 for the stack. So we decided to have a closer look at these sintered discs to see what the problem might be and why the quality factor seemed so low. One SM-111 disc was mounted to a small 3/8 inch diameter aluminum cylinder and then placed inside an electron microscope. We obtained the following images. See Figure 4.8. There appear to be a great deal of voids present in this sintered powered material. This could account for the low quality factor measured.

For comparison we decided to purchase some sintered discs from a different vendor, APC international [16] and also look at these under an electron microscope. Some PZT discs, material APC-844, (19mm diameter and 2mm thick) were purchased and examined under the electron microscope. The APC material also has some desirable properties, the reported Q_m was 1500. The electron microscope photographs are shown in figure 4.9.

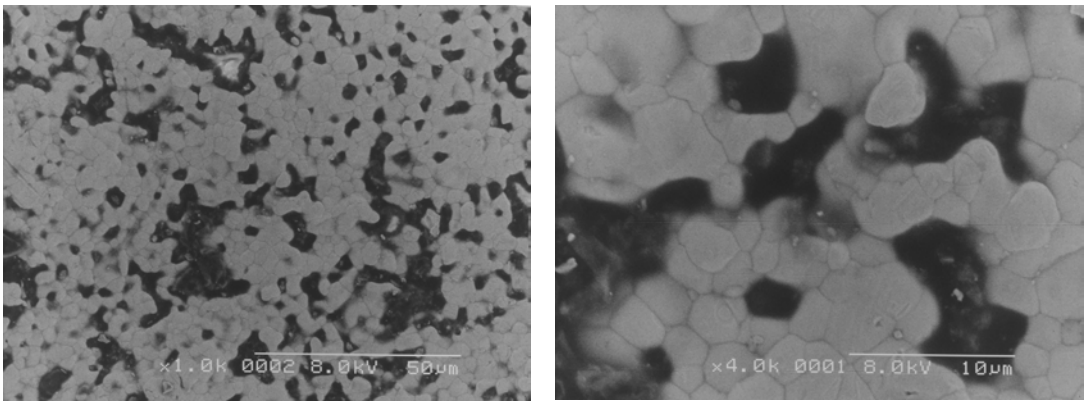

Figure 4.8 Electron microscope images of a 19mm diameter disc of SM-111. No etching was done, the only preparation was a simple wipe with an alocohol swab. The disc had a silver coating used as an electrode. This was considered sufficient and no further conductive coating was needed. On the left the photograph shows a scale of 50 microns. On the right the scale is 10 microns. The dark spots are voids in the material.

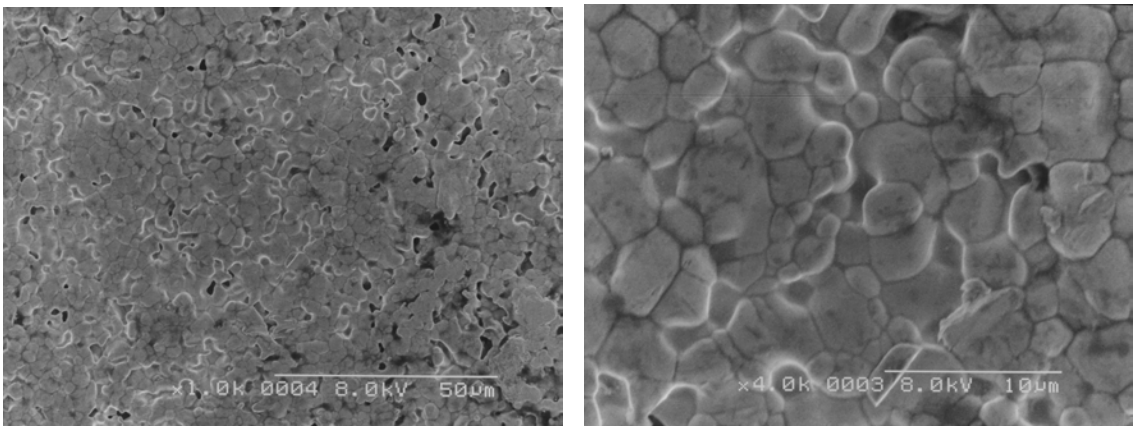

Figure 4.9 Electron microscope images of a 19mm diameter disc of APC-844. No etching was done, the only preparation was a simple wipe with an alocohol swab. The disc had a silver coating used as an electrode. This was considered sufficient and no further conductive coating was needed. On the left the photograph shows a scale of 50 microns. On the right the scale is 10 microns. The dark spots are voids in the material. Note that there are considerably fewer voids than in the photographs in Fig.10. The slight glow is caused by electron discharge, the silver coating may not have had a good ground to the small aluminum mounting bracket in this case.

The APC 844 has very similar properties to SM-111. Curie temperature is also 320 degree C, dissipation given by tan δ =0.4 , piezoelectric constant d_{33}= 300 x10^{-12} m/V, Young's modulus Y_{33}=6.3 x10^{10} N/m^2 and density of 7.7 g/cm^3. It appears that the sintering of the APC material is superior to the SM discs. The failure of conductive cracks in thermally depoled PZT-4 ceramics have been studied by Zhang et al [17]. We also would like to try crystal discs rather than sintered. We are currently waiting for our first shipment of crystal PIN-PMN-PT, (TRSX4B), from TRS technologies.

There are multiple paths forward regarding the quality of materials. Using a different manufacturer is one and moving up to crystal discs is another. Both options will be tested. The reason for wanting the high quality factor is because the force produced by the device has been

shown in a model to scale with the Q_m factor [18,4], see section 5 below. To make the point, we include two plots by JJAR using his model to predict the force at various Q_m values. See figure 4.10 and 4.11 which use different damping models. Also note that both models predict a change of direction in the force close to the resonant frequency, which we showed experimentally in figure 4.6.

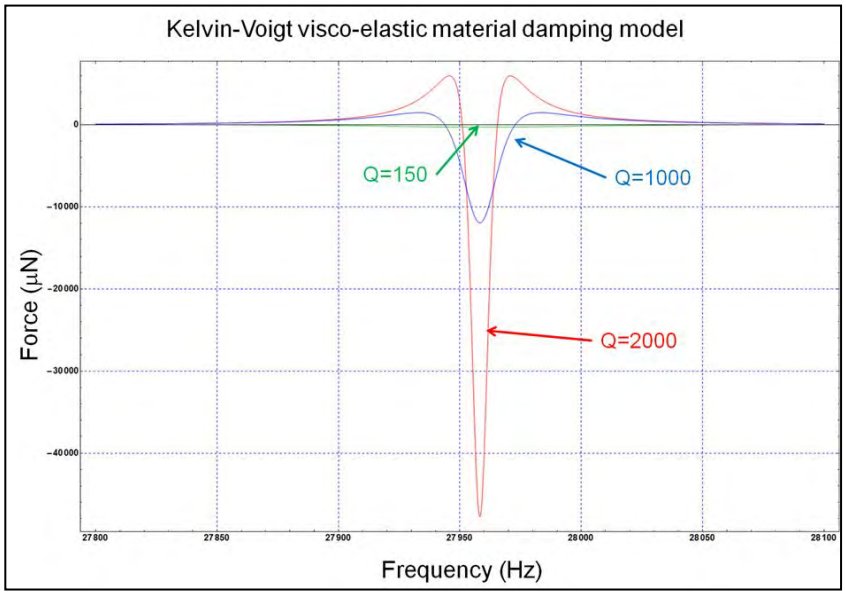

Figure 4.10 Plot of frequency in Hz verse force in micro Newtons for various Q_m values. These plots were using a Kelvin-Voigt damping model.

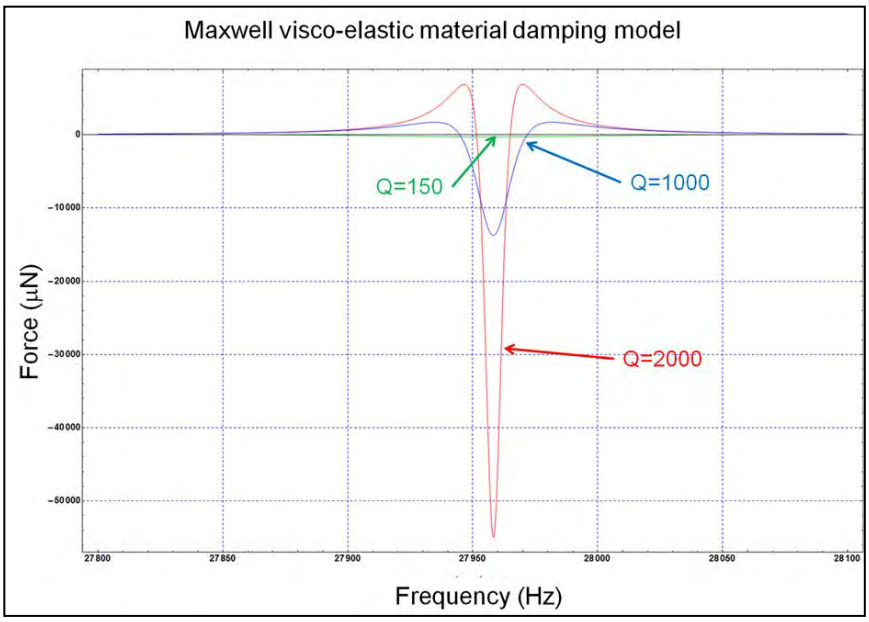

Figure 4.11 Plot of frequency in Hz verse force in micro Newtons for various Q_m values. These plots were using a Maxwell visco-elastic damping model.

It also came to out attention, that if we are to try expensive crystals we would want to make sure that our mounting brackets are capable of evenly distributing the pressure, from the bolts, over the surface of the crystal so as not to crack them. So far we have been using flat surface brass and aluminum end masses. We decided to test the pressure distribution using Fuji-film, a pressure sensitive film [19]. The stress σ can be calculated as follows,

$$\sigma = \frac{N\tau}{A\mu_f d_{bolt}} = 793.77\tau \tag{19}$$

where N is the n umber of 2-56 bolts (N=6) , τ is the torque on the bolts (in-lbf), A is the area of the PZT (which is 0.4395 in^2), μ_f =0.2 the coefficient of friction between stainless steel and brass, and bolt diameter d_{bolt} =0.086 in (for 2-56 ANSI screws). Hence we can form a table of values for the stress given a certain torque on the bolts. See Table 1.

Table 1. Stress for a given torque

Torque τ in (in-lbf)	Stress σ (psi)
3	2381
4	3175
5	3969
6	4762

The Fujifilm pre-scale comes in different pressure ratings, it was determined that medium (MS rating 1,400-7,100psi) would be best for our application. The high (HS) film has a rating of (7,100-18,500 psi). The results of our test are shown in figure 4.12. The distribution of pressure was far from even. We instead got a contact ring around the edge where the 6 bolts were located. The test shows we certainly have room for improvement. The outside pressure was measured to be quite high ~ 7,300 psi. A way forward would be to profile the brass and aluminum end caps in a domed shape to more evenly distribute the pressure from the bolts. We might also try using Kapton film as a gasket between the PZT stack and the end masses.

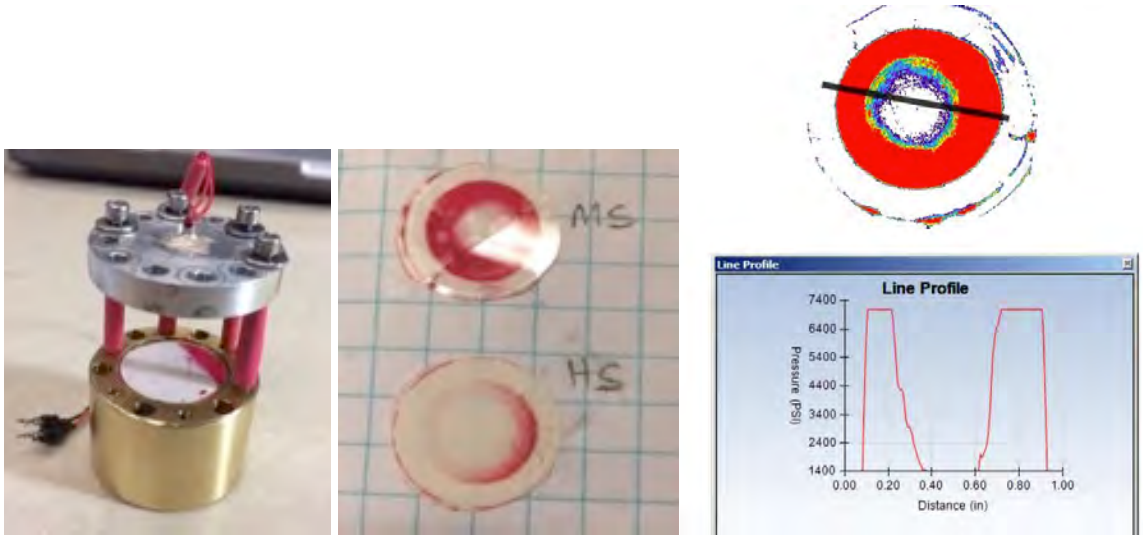

Figure 4.12 The test rig on the left and the actual film used in the center. The medium sensitive pressure film was seen to be the best fit (the high sensitive pressure film was discarded). On the right is a "color" version of the medium film, with a detailed cross section given of the pressures.

In order to correct for this highly asymmetric pressure distribution we utilized contact mechanics and found the correct dome profile (h) for the end masses in contact with the disc crystals should be,

$$h = \ell n\left[\sqrt{1-\frac{x^2}{R^2}}\right] \tag{20}$$

which is plotted in figure 4.13. The dome height was estimated to be 0.8 thousandths of an inch. The profile is calculated from contact mechanics of a rigid flat punch on an elastic half space, see for example [20]. This is known as a Boussinesq problem [21,22].
In the text [20], equation (2.66) is when the x>a, where a=R is the radius of the disc. So $(x/a)^2$ -1 would become $1 - (x/a)^2$ for when x<a=R.

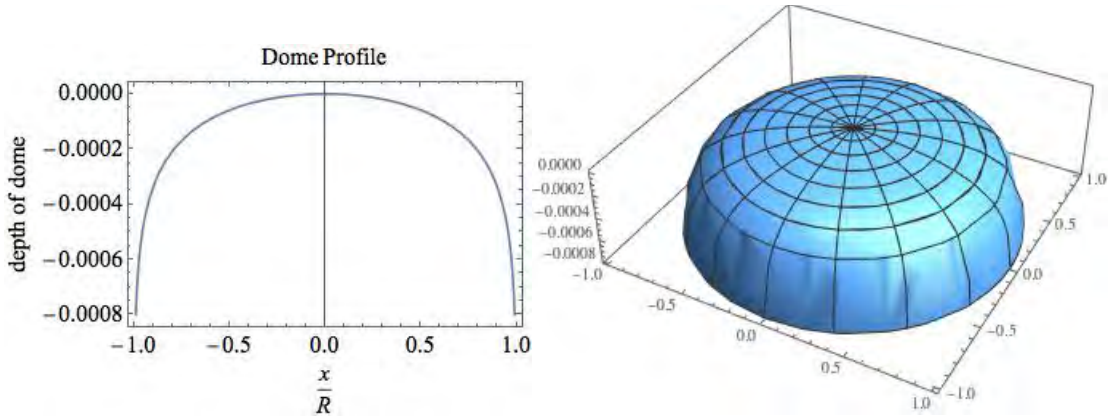

Figure 4.13 This is the profile of the end masses, both brass and aluminum. Both are in contact with the PZT stack**.** We tested this profile using only the machined brass side and found that the Fujifilm gave a

much more even distribution of pressure and the pressure (at 4 in-lbfs torque on the bolts) was reduced to 3057 psi.

To calculate the thickness of the gasket between the stack and the end masses, we should first analyze the indentation of a flat axisymmetric punch on an elastic half plane. Using again σ as the average contact stress,
$F= \sigma \pi R^2$ as the contact force, $E\cong 2 \times 10^6$ lbf/in^2 as the modulus of elasticity (smaller due to porosity of the SM-111), $\nu=0.3$ as the Poisson ratio, R=0.3740in (8.5mm) as the radius of contact area and Δ as the deflection (in inches). Then

$$\Delta = \frac{F}{2R\left(\frac{E}{1-\nu^2}\right)} = 0.0008 \qquad (21)$$

which explains our choice of the dome height.

5. Analytical solution of the partial differential equations for the Mach Effect drive, including piezoelectricity, electrostriction and viscoelasticity (by José J. Rodal, Ph.D.)

Continuum mechanics model: analytical solution of the partial differential equations

The piezoelectric stack is modeled as possessing both inertial mass and viscoelastic stress-strain properties that are continuously distributed through the piezoelectric stack length. No assumption is made of lumped property elements like massless dashpots, massless springs or rigid point masses in the piezoelectric material, instead partial differential equations of continuum mechanics are solved in the complex domain. The piezoelectric stack is modeled as a viscoelastic rod where initially plane cross sections (in the undeformed configuration) remain plane after deformation, such that material particles move only in the longitudinal direction of the rod. The effect of lateral displacements upon longitudinal motions is neglected: it is assumed that transverse shear, torsional, and bending deformations are negligible when compared to the axial deformation.

This continuum-mechanics description leads to a partial differential equation in terms of time and material position (using a Lagrangian coordinate system) which must be satisfied at every point subject to initial and boundary conditions. Under these assumptions, the boundary value problem becomes an eigenvalue problem when the differential equation of motion is homogeneous (i.e when the right hand side forcing function is set equal to zero), in which case nontrivial solutions exist in terms of parameters called eigenvalues. Since the piezoelectric stack is analyzed as a continuum, the system has an infinite number of degrees of freedom, and hence an infinite number of natural modes (eigenmodes) and frequencies of vibration (eigenfrequencies). It is assumed that strains are small (a very valid approximation since piezoelectric strains are infinitesimal) and hence that the strain-displacement relationships are linear. The (force per unit volume)

equilibrium equation follows from the assumption that the transverse shear stress is negligible and that there is negligibly small body force.

Two viscoelastic constitutive models are considered. In the first constitutive model the constitutive equation relates the longitudinal stress component to the longitudinal strain component and its time derivative (the strain rate). This model is known as the Kelvin-Voigt model, and for this model the constitutive properties are an elastic modulus and a characteristic relaxation time (in viscoelasticity, the term relaxation time is used for imposed strain or strain-rate conditions while retardation time is used for imposed stress or stress-rate conditions, we use the term relaxation time in general to denote the time constant associated with exponential time decay: the time that it takes for the signal to decay to a factor of 0.368 of its original amplitude). The second viscoelastic constitutive model relates the time derivative of the longitudinal stress component (the stress rate) to the time derivative of the longitudinal strain component (the strain rate) and to the stress. This model is usually known as a Maxwell model, and the constitutive properties are a hypoelastic modulus and a characteristic relaxation time. (In this model the modulus is hypoelastic since it relates the stress-rate to the strain-rate, rather than relating the stress to the strain).

Differentiating the constitutive equations with respect to the longitudinal coordinate and using the strain-displacement equation, and using the equilibrium equation to express the stress component in terms of the displacement, results in a partial differential equation for the displacement as a function of time and the longitudinal coordinate. When integrating this equation, deliberately, we do not use the usual Maxwell model (which would lead to a viscoelastic *fluid* model) but instead use the integration constant to obtain a viscoelastic *solid* material model that has fluid viscous damping. In other words, upon integrating this equation, the hypoelastic stress-rate strain-rate relationship integrates to an elastic modulus stress-strain relationship (that defines a solid material). Therefore we end up with two different *solid* viscoelastic models. For small values of damping, both models converge to the same acoustic equation of wave propagation of a dynamic elastic solid. The two models only differ in the representation of the damping term: the first model (a Kelvin-Voigt solid viscoelastic damping model), has a damping term proportional to the gradient of the strain rate, while the second model (the fluid damping model) has a damping proportional to the velocity. The relaxation time for the Kelvin-Voigt model occurs in the numerator of the damping term, while the relaxation time occurs in the denominator of the damping term: this results in inverse (to each other) damping behaviors with respect to frequency, for a given value of relaxation time.

In general, materials have a distribution of relaxation times, so each material model being represented with only one relaxation time (as in the present model) may be used in a narrow distribution of frequency. At a fixed temperature, the first model (a Kelvin-Voigt model) is appropriate to describe behavior below a frequency transition point, such that damping increases with increasing frequency, while the second damping model is appropriate to describe behavior above it, such that damping decreases with increasing frequency. At a fixed frequency, assuming that time-temperature superposition of a linear viscoelastic material applies, the second model (the fluid damping model) is appropriate to describe behavior below a temperature transition point, such that damping increases with increasing temperature, while the fist model (the Kelvin-Voigt damping model) is appropriate to describe behavior above it, such that damping decreases with increasing temperature.

The model, in addition to the viscoelastic terms, incorporates additive piezoelectric and electrostrictive components, by additively decomposing the total strain into piezoelectric, electrostrictive and viscoelastic components (where the viscoelastic components can be due to either of the two viscoelastic models considered). For the electrostrictive and piezoelectric components, the electric field is related to the electric potential. A linear variation of the electric potential through the (thin) thickness of the plates that form the sandwich stack is considered. Therefore a constant electric field through the (thin) thickness of each plate that forms the sandwich stack is considered.

The piezoelectric Langevin stack is modeled as a sandwich of piezoelectric plates connected electrically in parallel and mechanically in series, with the (brittle) piezoelectric plates held in compression between two end metallic masses by screws under tension. We account for the effective increase in stiffness and mass of the piezoelectric stack due to these screws, in the equations of motion, by defining an effective mass per unit length and an effective longitudinal stiffness taking into account the mass densities of the stack components: the piezoelectric plates, the electrodes, the adhesive and the screws, and their respective cross-sectional areas, as well as their respective moduli of elasticity (in the thickness direction of the piezoelectric plates), effective length of the screws, and the number of screws. Therefore, the effect of the screws is taken into account in the equations of dynamic force equilibrium for the Kelvin-Voigt and fluid damping models, and therefore it is also taken into account in the effective speed of sound of the stack.

Two fundamentally different support conditions are modeled: the device in a spaceship in space (the spaceship having free boundary conditions) and the device in a laboratory experiment. The laboratory experiment is modeled such that the bottom mass of the stack is attached by a bracket to a torsional pendulum to measure forces, therefore incorporating an attachment spring and damping constant due to the support, while when we model the system in space, we take the values of the support spring and support damping constant to be equal to zero.

Notice that for both support models the equation of motion and boundary conditions constitute a system that is *not scleronomic*: since time appears in the constraints. Also notice that the system is *not holonomic* either: the constraints involve velocities and acceleration. Since the end constraints involve velocities and accelerations, the response will involve a mixture of displacements and forces, and hence, in general, an analytic solution cannot be readily obtained by a series expansion of orthogonal mode functions. Therefore, to obtain an analytic solution, a harmonic input in the complex domain is applied to obtain a steady-state harmonic response expressed in terms of the spatial, time and frequency response function components.

The steady-state harmonic response function for the displacement is analyzed as a superposition of a harmonic piezoelectric excitation plus an electrostrictive harmonic excitation at twice the frequency of the piezoelectric excitation.

The solutions for both damping models (the Kelvin-Voigt damping model and the fluid damping model) can be expressed in terms of a frequency-dependent damping ratio (the ratio of the actual damping coefficient to the critical damping coefficient) or, alternatively, in terms of a frequency-dependent quality factor of resonance.

It can be shown analytically, that for small values of the damping ratio, at constant temperature, the damping increases with frequency for the Kelvin-Voigt viscoelastic solid model, while the damping decreases with frequency for the fluid damping model. The analytical solution is arrived at, after transforming variables into a dimensionless form, solving for parameters that are complex valued functions of frequency. The value of these parameters must be obtained by satisfaction of the boundary conditions.

Decoupling of stack from the torsional pendulum's holding bracket's stiffness and damping

The analytical solution shows that the spring stiffness due to the bracket holding the stack to the torsional pendulum, by the end mass, ceases to be relevant when the natural frequency due to the square root of the stiffness (per unit length) of the compressed piezoelectric stack divided by the end mass (the brass mass) attached (by the holding bracket) to the torsional pendulum is significantly lower than the excitation frequency. For example, for a brass mass of 0.1 kg and an excitation frequency of 30 kHz, this means that the holding spring is irrelevant if the spring stiffness (defined as force divided by displacement) of the holding bracket is significantly smaller than 3.55×10^9 N/m.

Similarly, the analytical solution shows that the effective damping of the bracket holding the stack to the torsional pendulum, by the lower mass, ceases to be relevant when it is significantly smaller than the longitudinal stiffness divided by the speed of sound of longitudinal waves of the piezoelectric stack. For example, if the stiffness (defined as elastic modulus times cross-sectional area) of the compressed piezoelectric stack is 2×10^7 N, and the speed of sound of longitudinal waves of the piezoelectric stack is 3000 m/s, it follows that if the effective damping of the bracket holding the stack to the torsional pendulum is significantly lower than 6600 N/(m/s), the effective damping of the bracket associated with holding the stack by the lower mass is irrelevant.

The spring stiffness and the effective damping of the bracket associated with holding the stack by the lower mass cease to be relevant for the same conditions for fluid damping as for the Kelvin-Voigt damping model decoupling conditions previously discussed.

Numerical results

As previously discussed, the solution is based on continuum mechanics, therefore the solution has effectively an infinite number of degrees of freedom, and hence all eigenfrequencies and eigenmodes of the piezoelectric stack can be solved for. The solution is very sensitive to the type of damping mechanism in the piezoelectric stack and to the mass distribution of the Langevin stack (the end masses play a significant role).

The following plots show the thrust force vs. the excitation frequency for the Kelvin-Voigt viscoelastic solid damping model and for the fluid damping viscoelastic solid model, both based on a piezoelectric stack with a quality of resonance factor Q equal to 60, an aluminum end mass of 7.29 g and a brass end mass of 60 g, supported by a compliant bracket connecting it to the torsional pendulum (and hence effectively decoupled from it, as discussed in the previous section). In the interest of saving space, the figures are given for a piezoelectric material with elastic modulus and

mass density ratio that results in the displayed resonance frequencies, the principal first natural frequency being slightly over 30 kHz (a stiffer material would result in a higher natural frequency). The thrust force is nearly zero except near the natural frequency. Two principal natural frequencies are shown to occur in the range of 0 to 100 kHz, displayed in a linear scale in the horizontal axis, the first mode shape being due to the two end masses behaving as if they were connected by a spring, with oscillations moving towards each other and away from each other in a harmonic motion. The second main mode shape, at a frequency exceeding 75 kHz, has the stack behaving as a three lumped mass system with the additional motion of the center of the piezoelectric stack moving harmonically with respect to the two end masses.

Examining the behavior of the thrust force vs. frequency, as the frequency is increased starting from zero, the absolute magnitude of the thrust force only significantly deviates from zero near the natural frequencies, exhibiting first a small force (about 0.4 microNewtons) directed towards the brass mass, that quickly changes direction near the natural frequency, where a peak value of near 4.6 microNewtons is reached at 30 kHz, in the direction towards the aluminum mass. As the frequency is further increased, the thrust force rapidly decreases and changes direction, reaching a much smaller peak (almost 0.8 microNewtons) directed towards the brass mass. Increasing the natural frequency the force rapidly decreases to zero. While this 30 kHz natural frequency appears to be mainly piezoelectric in nature, there are smaller (less than 1 microNewton) amplitude natural frequencies at about 38 kHz and at about 62 kHz that appear to comprise electrostrictive resonance as well. The behavior at 38 kHz shows two similar peak responses, the first one slightly below 38 kHz with the force directed towards the aluminum mass, and the second slightly above 38 kHz with the force directed towards the brass mass. The behavior at 62 kHz is opposite: slightly below 62 kHz the force is directed towards the brass mass, and slightly above 62 kHz the force is directed towards the aluminum mass. The second main natural frequency near 75 kHz (behaving as a three lumped mass system with the center mass connected to the two end masses by two springs) exhibits a force increasing from zero as one increases the frequency, reaching a thrust force of 0.3 microNewtons toward the aluminum mass, then decreasing to zero as one further increases the frequency and changing direction in the opposite direction reaching a peak of 0.6 microNewtons in the direction towards the brass mass, and then decreasing to zero as one further increases the frequency.

The fluid damping viscoelastic solid model shows a similar behavior as the Kelvin-Voigt viscoelastic solid damping model for the first natural frequency at 30 kHz, but a radically different behavior for the second main natural frequency near 75 kHz. While the Kelvin-Voigt viscoelastic solid damping model shows much higher amplitude for the lower mode shape, the opposite is the case for the fluid damping viscoelastic solid model. The second main natural frequency near 75 kHz (behaving as a three lumped mass system with the center mass connected to the two end masses by two springs) exhibits first a force of around 4.5 microNewtons directed towards the aluminum mass, that changes direction near the natural frequency, where a peak value of nearly 30 microNewtons is reached, in the direction towards the brass mass. As the frequency is further increased, the thrust force rapidly decreases and changes direction again, reaching a much smaller peak (almost 3 microNewtons) again directed towards the aluminum mass. Increasing the natural frequency the force rapidly decreases to zero.

The fluid damping model also shows the smaller (less than 1 microNewton) amplitude natural frequencies at about 38 kHz and at about 62 kHz that appear to comprise electrostrictive nature as

well. The behavior for these natural frequencies is similar to the Kelvin-Voigt model. The behavior near 38 kHz shows two similar peak responses, the first one slightly below 38 kHz with the force directed towards the aluminum mass, and the second slightly above 38 kHz with the force directed towards the brass mass. The behavior at 62 kHz is opposite: slightly below 62 kHz the force is directed towards the brass mass, and slightly above 62 kHz the force is directed towards the aluminum mass.

It is evident that (as expected) the Kelvin-Voigt viscoelastic solid damping model results in much higher damping of higher natural frequencies than the fluid damping model: notice that the thrust force for the 2nd natural frequency for the Kelvin-Voigt viscoelastic solid damping model is significantly smaller than the thrust force for the 1st natural frequency. The opposite is the case for the fluid damping model.

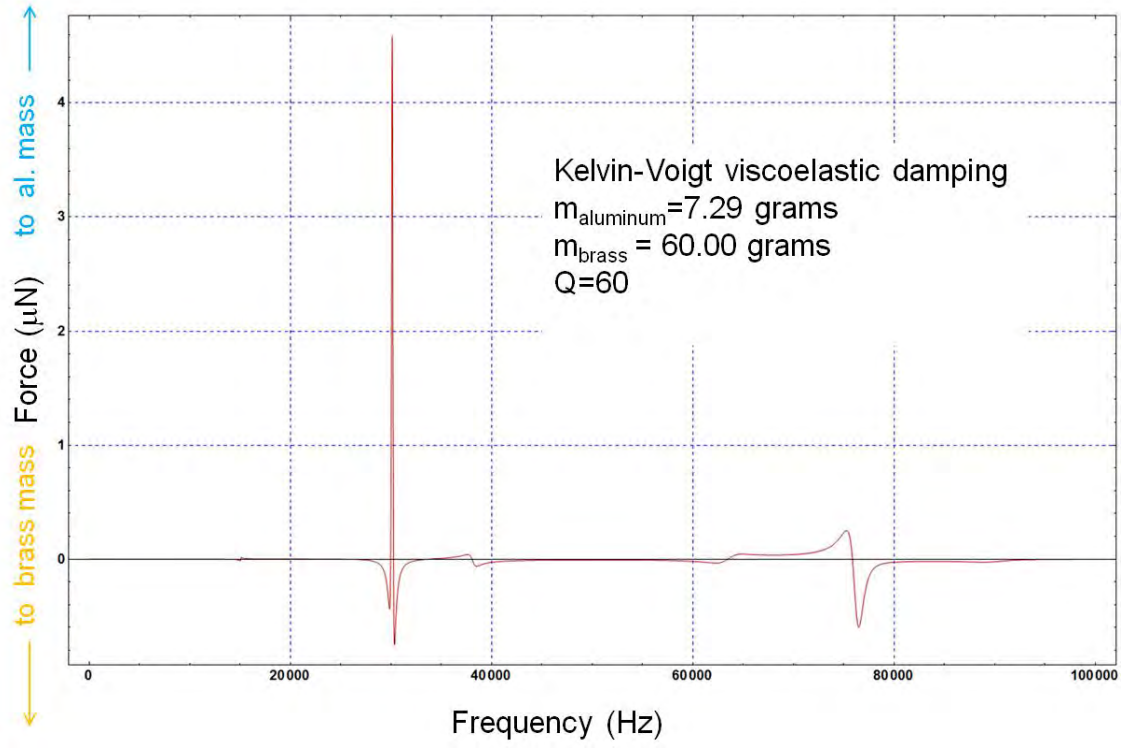

Figure 5.1 Thrust force (microNewtons) vs. frequency (Hertz) for the Kelvin-Voigt damping viscoelastic solid model, showing the first two natural frequencies.

Alt Text Fig. 5.1:

This is a line plot showing the thrust force (microNewtons) in the vertical axis vs. frequency (Hertz) in the horizontal axis, for the Kelvin-Voigt viscoelastic damping model. This plot is explained in the main text.

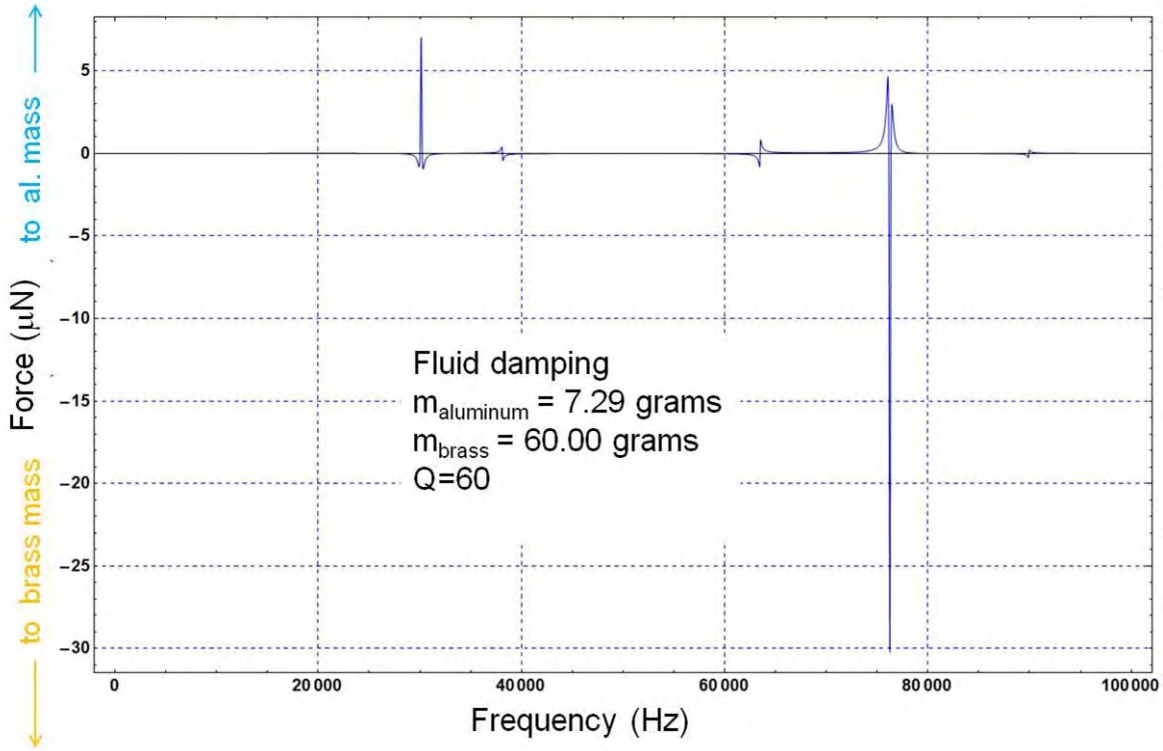

Figure 5.2 Thrust force (microNewtons) vs. frequency (Hertz) for the fluid damping viscoelastic solid model, showing the first two natural frequencies.

Alt Text Fig. 5.2:

This is a line plot showing the thrust force (microNewtons) in the vertical axis vs. frequency (Hertz) in the horizontal axis, for the fluid damping viscoelastic solid model. This plot is explained in the main text.

It is interesting to explore the behavior of the thrust force as a function of the mass of the big end of the Langevin stack, keeping everything else constant. Therefore we show next the plots for the thrust force (in microNewtons) vs. the mass (in kilograms) of the brass mass, for a piezoelectric stack with an aluminum mass kept constant (at 10 g for the first two plots, and 7.29 g for the final two plots) supported by a compliant bracket connecting it to the torsional pendulum. The portion of the aluminum bracket that is bolted to the brass mass is modeled as a constant 4.21 g for this analysis, so that the big end mass is effectively 4.21 g plus the brass mass. Therefore both ends of the Langevin stack have equal total masses (and therefore the thrust force is zero) when the brass mass is 5.79 g for the 10 g aluminum mass case and when the brass mass is 3.08 g for the 7.29 g aluminum mass case.

There are two curves shown in these plots: a blue curve and a red curve. As described previously, the thrust force behavior at frequencies near a natural frequency display thrust force peaks in

opposite directions, depending on how close the excitation frequency is to the natural frequency, towards the aluminum end mass and towards the brass end mass. The curves in the following plots show the peak thrust response near the first principal natural frequency. When examining the following plots it has to be taken into account that the frequency at which this first principal natural frequency takes place changes as a function of the mass of the brass end: the higher the mass, the lower the natural frequency, the lower the mass, the higher the natural frequency (as the natural frequency is a function of the square root of the reduced mass). The blue curve shows the peak response directed towards the aluminum end mass and the red curve shows the peak response directed towards the brass end mass. Notice that for the following figures the horizontal scale (displaying the mass) is displayed as a logarithmic scale, in order to be able to show the behavior for a small end mass as well as the behavior for a large end mass (relative to the mass of the piezoelectric stack), for example: the mass of a spaceship. It is shown that the thrust force is still finite, even when applied to a large mass. Both damping models show a quick asymptotic convergence to a thrust force value for large end mass. The Kelvin-Voigt viscoelastic solid damping model is less sensitive to the value of the end mass and results in a slightly higher thrust force for large end mass than the fluid damping model.

For comparison with the numerical solution of this continuum mechanics viscoelastic-piezoelectric-electrostrictive model, consider the experimental data discussed in pages 104 and 105 of Fearn and Woodward's article [H. Fearn and J. Woodward, "Experimental Null Test of a Mach Effect Thruster," Journal of Space Exploration, Volume 2, Issue 2, (2013), pp. 98-105. https://physics.fullerton.edu/~heidi/JSE13.pdf]:

> "If we were to place identical brass masses on either side of our active PZT stack, then the mass fluctuations would result in pushes and pulls of equal magnitude and the device should just oscillate a little but show no average thrust. This was deemed to be worth testing. It would show that we were able to eliminate any unwanted vibration, noise effects. 0.635 cm length brass masses were attached to either end of the PZT stack. A symmetric arrangement for the mount was used so as not to bias the forces in either direction. A central aluminum mounting ring with 3 screws arranged at 120 degree intervals which contacted plastic tabs glued onto the PZT stack performed this function. Care was taken not to short any of the electrodes which were embedded in between the PZT disks. See also the black heat shrink which was wrapped around each of the 4-40 threaded rods used to bind the device together... The results for the resonant frequency 42.4 kHz are shown in Figure 7. Both forward and reversed runs were acquired and averaged. Note that the thrust does not reverse direction in this case, as is shown in Figure 7c. It is clear that if the higher power result shows a null in the thrust then so will the lower power result, which was indeed the case... Clearly any thrust signal has been lost, and all that remains is noise, or a small oscillation on top of the noise due to the resonant frequency of the device. "
>
> "In addition, it was determined that an optimal brass reaction mass is necessary to give maximal thrust. Several different brass reaction masses 64.7 g, 80.9 g, 96.8 g, 112.6 g and 128.3 g were tried. We found that for this PZT stack, the preferred brass reaction mass 80.9 g."

There is good agreement with this scant data set for: equal end masses (for which the model shows, as expected, no thrust force), and for a brass mass of 65, 81, 97, 113 and 128 grams.

Notice that the behavior of the thrust force for a piezoelectric stack with end masses that are nearly equal is extremely sensitive to the precise value of the end masses. Both models show an optimal end mass for which the thrust force is maximized, this end mass being a little smaller than 0.1 kg, in agreement with the experimental results. The fluid damping model shows a sharper peak force vs. mass behavior, and a value of this mass closer to experiment. Both models show that for a brass mass larger than twice the aluminum mass, the maximum thrust force occurs in the direction towards the smaller (aluminum) mass. For a brass mass approximately equal to the aluminum mass, the maximum thrust force occurs in the direction towards the brass mass. The fluid damping model show a significantly larger peak thrust force (in the direction towards the brass mass) for a small brass mass (while the Kelvin-Voigt viscoelastic solid model does not show as much this behavior). The thrust force is zero when the two ends (attached to the piezoelectric stack) have the same mass (taking into account the portion of the aluminum bracket -kept constant at 4.21 g for this analysis- that is bolted to the brass mass).

Unfortunately no experiments have yet been conducted with a small brass end mass to verify this numerical solution. It would be interesting to conduct experiments with such small brass end masses, in order to characterize the viscoelastic damping of the piezoelectric materials being tested, to assess the continuum-mechanics model and to maximize the thrust (as well as to maximize the ability to reverse the thrust direction by changing the excitation frequency).

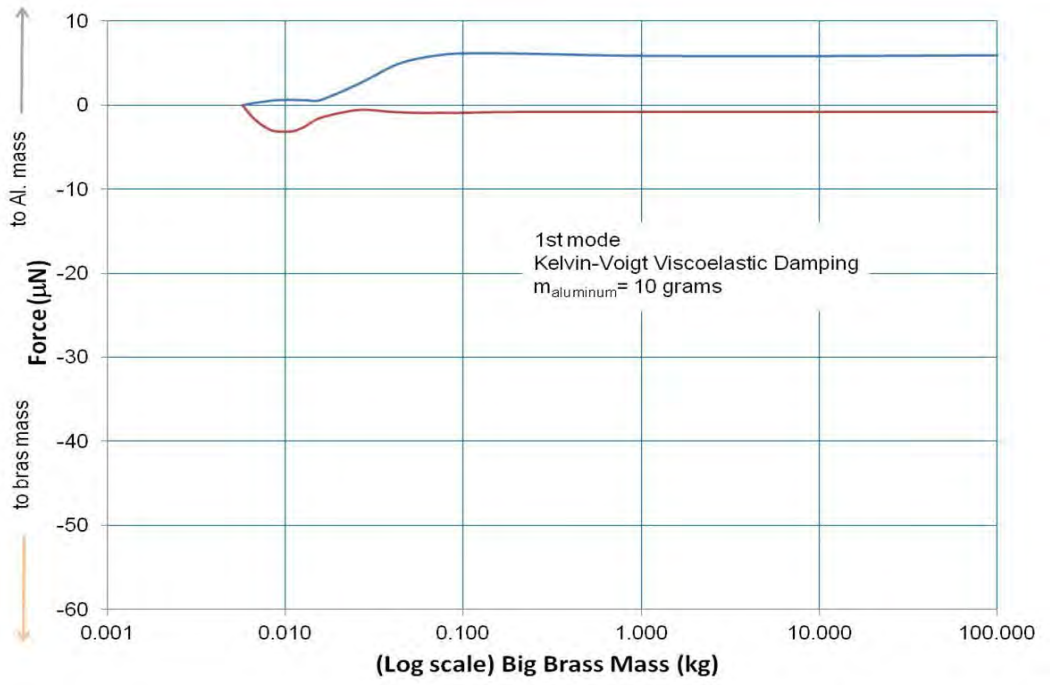

Figure 5.3 Thrust force (microNewtons) vs. big brass mass (kg) at the first principal natural frequency for the Kelvin-Voigt damping viscoelastic solid model, for a fixed small aluminum mass end of 10 g.

Alt Text Fig. 5.3:

This is a line plot showing the thrust force (linear scale, in microNewtons) in the vertical axis vs. frequency (logarithmic scale, in Hertz) in the horizontal axis, for the fluid damping viscoelastic solid model. The plot is explained in the main text.

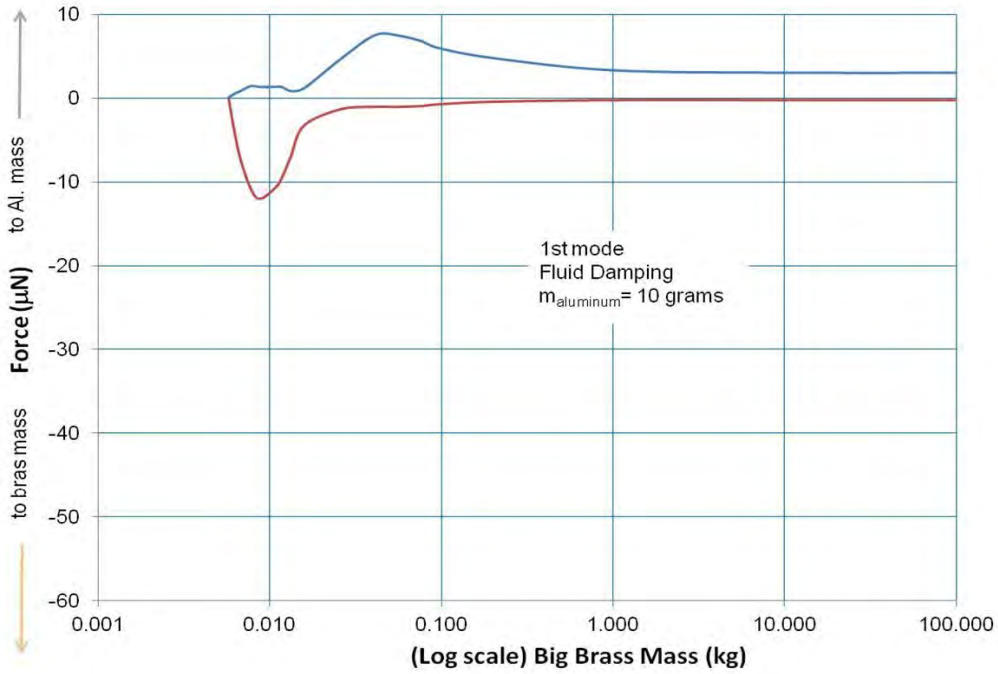

Figure 5.4 Thrust force (microNewtons) vs. big brass mass (kg) at the first principal natural frequency for the fluid damping viscoelastic solid model, for a fixed small aluminum mass end of 10 g.

Alt Text 5.4:

This is a line plot showing the thrust force (linear scale, in microNewtons) in the vertical axis vs. frequency (logarithmic scale, in Hertz) in the horizontal axis, for the fluid damping viscoelastic solid model. The plot is explained in the main text.

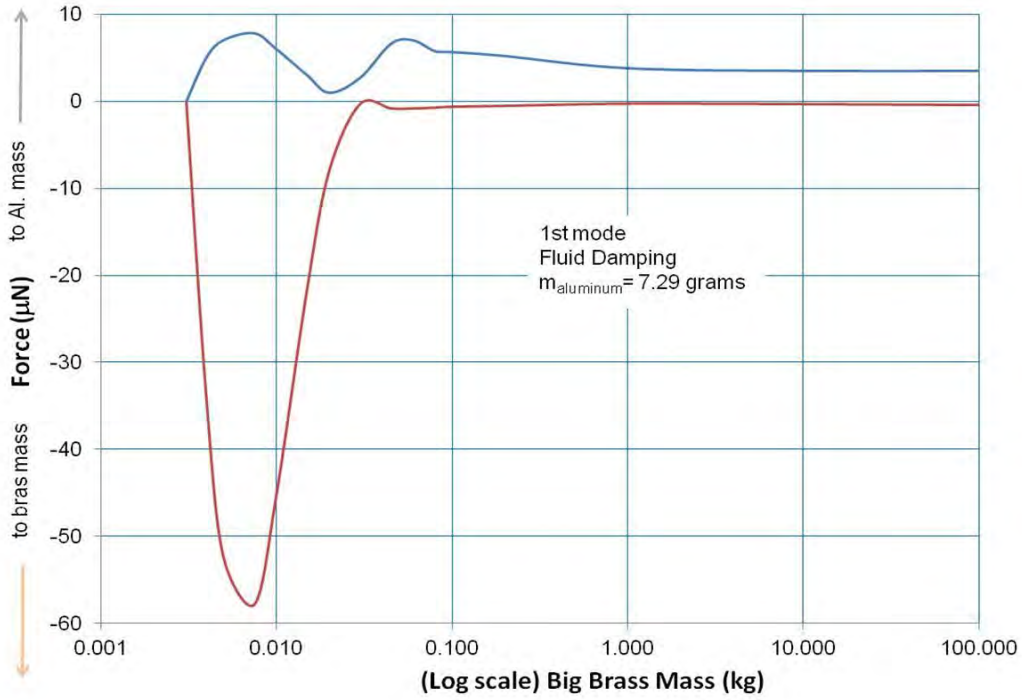

Figure 5.5 Thrust force (microNewtons) vs. big brass mass (kg) at the first principal natural frequency for the fluid damping viscoelastic solid model, for a fixed small aluminum mass end of 7.29 g.

Alt Text Fig. 5.5:

This is a line plot showing the thrust force (linear scale, in microNewtons) in the vertical axis vs. frequency (logarithmic scale, in Hertz) in the horizontal axis, for the fluid damping viscoelastic solid model. The plot is explained in the main text.

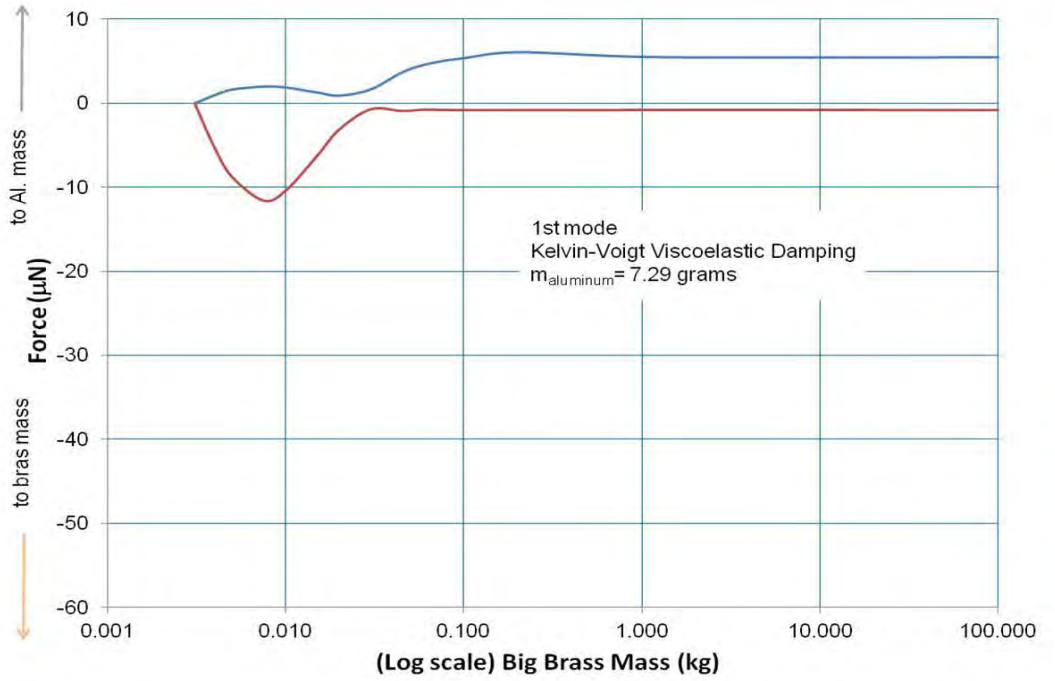

Figure 5.6 Thrust force (microNewtons) vs. big brass mass (kg) at the first principal natural frequency for the Kelvin-Voigt damping viscoelastic solid model, for a fixed small aluminum mass end of 7.29 g.

Alt Text Fig. 5.6:

This is a line plot showing the thrust force (linear scale, in microNewtons) in the vertical axis vs. frequency (logarithmic scale, in Hertz) in the horizontal axis, for the fluid damping viscoelastic solid model. The plot is explained in the main text.

6. Preliminary mission suggested to the Solar Gravity Lens

As part of our NIAC work, we considered a suitable initial mission for the Interstellar Mach-Effect Spacecraft (IMES), and settled on a mission to the focus of the solar gravitational lens (which is the focus of another phase 1 NIAC 2017 research effort under Slava Turyshev). The IMES could first be sent to the solar gravity lens focus for a closer look at Proxima b before going there. The gravity lens focus forms a focal line starting at approximately 550 a.u. from Earth. (1 astronomical unit [a.u.] is the distance from the Earth to the sun). At this focus a distant source would form an Einstein ring about the Sun; at a distance of 550 AU this ring would be at the base of the solar corona, and this would be largely overwhelmed by light from the solar corona. Useful imaging with the solar gravity telescope would require being at a considerably larger distance from the Sun, several thousand a.u. to allow for a clean separation between a distant target and the solar flux.

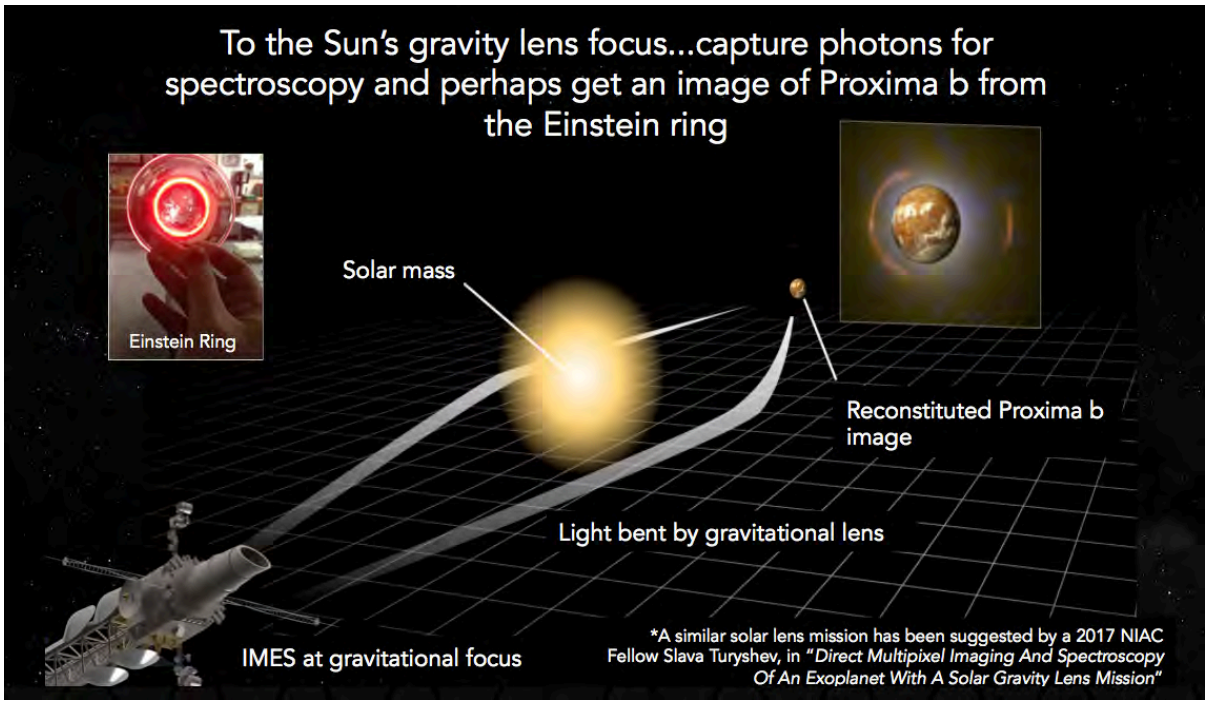

Figure 6.1 Solar gravity lens used to capture an image of Proxima b.

While in principle any distant source could be investigated by the IMES, a mission to Proxima Centauri would clearly benefit from more detailed prior knowledge, and we assume that IMES is sent to the antipodal point of Proxima to investigate Proxima b and its system. There are of course a number of engineering challenges that will have to be solved to obtain useful images and spectra from a gravity telescope; since these details are independent of the means of reaching the focal distance, and since the solar gravity lens project is the case study of another phase 1 NIAC 2017 fellow, we leave these details for that case study [23,24]. Also, any interstellar object coming into our solar system would be a natural target and worthy of further investigation, [25,26].

7. Probe Design & Shielding

7.1 Probe Design

The probe or interstellar Mach Effect spacecraft (IMES) is based on the model of Prometheus Jupiter icy moons orbiter (JIMO) [27]. We have slightly altered the design to incorporate MEGA drives at the position of the CoM of the spacecraft. The design feature a tri-plane configuration to reduce both the length and mass of the radiators and shielding. The truss is a triangular carbon fiber composite, capable of folding to a smaller dimension for launch. The radiators also would be designed to fold inwards for launch.

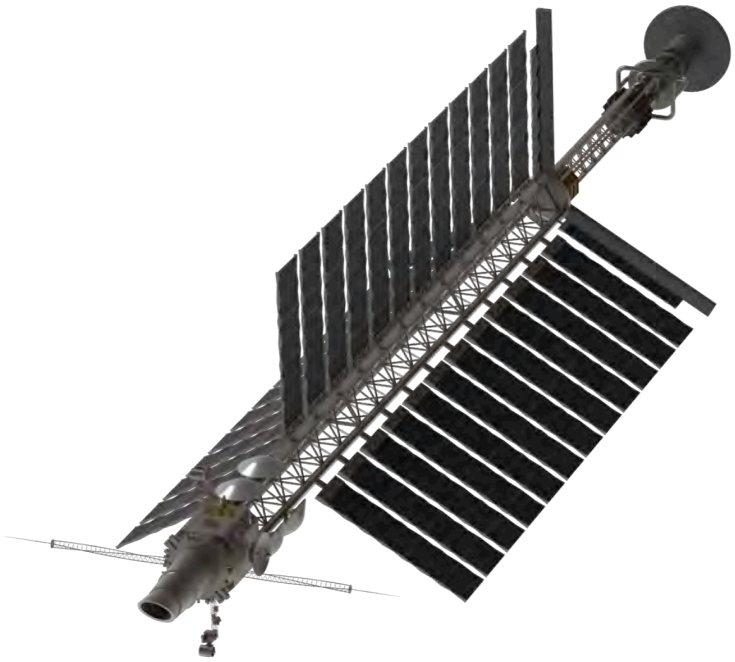

Figure 7.1 Interstellar Mach Effect Spacecraft (IMES) Design, named the SSI-Lambda. Cad Drawing by Tom Brosz from the Space Studies Institute.

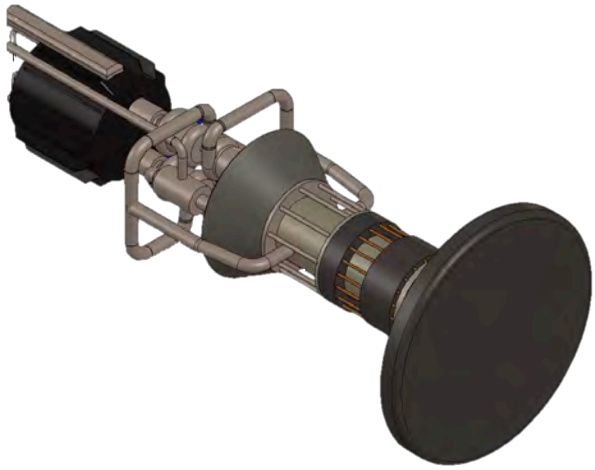

Figure 7.2 CAD drawing of the nuclear reactor at the front of the spacecraft, showing relativistic particle shield and 30 deg shadow shield for the reactor. Drawing by Tom Brosz.

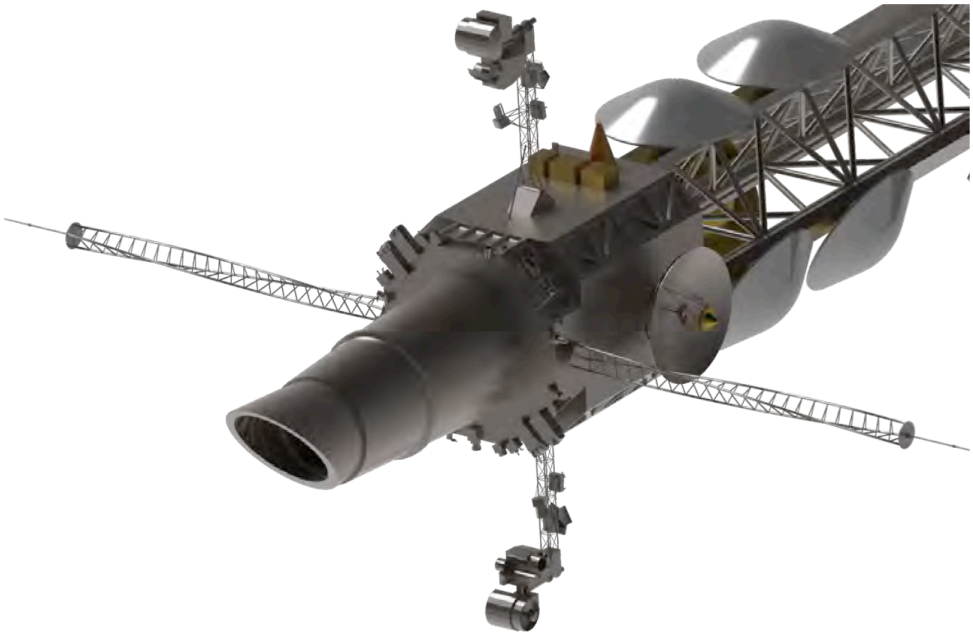

Figure 7.3 The rear end of the spacecraft. CAD drawing by Tom Brosz.

The dish shaped pods on the truss could be for a variety of scientific instruments or landers. The laser telescope is directly aft pointing back towards Earth. We envision a simple Lorri type telescope on a boom (stowed for travel along the truss) but able to swing out from the truss and look directly forward to pin point our destination once we slow down at about 100 a.u. distance from Proxima b.

7.2 Communications between Earth and the Probe

It is not enough to send a probe to another star system. Data will also have to be sent back.
• Here are the ground rules for my analysis:
◦ The mission target is Proxima Centauri, at 4.24 light years.
◦ The communications goal is 1 Gigabyte per year.
◦ I assume that all communications will be done as free-space optical communications using lasers.
◦ Efficiencies are all 80%, including detector quantum efficiencies.
◦ The laser systems are based on the Lunar Laser Communication Demonstration flown on LADEE in lunar orbit [28], and on ongoing work at JPL.
◦ A solid state Nd:YAG laser operating at 1064 nanometers is assumed.
◦ Pulse widths are assumed to be 100 picoseconds in duration.
◦ I assume a mode-locked laser maintaining coherency between pulses.
◦ The spacecraft has a telescope with a total collecting area of 1 m^2, a diameter of 1.26 m and a diffraction limited resolution of 844 nanoradians (10.4 arc minutes).

Some Physical Limits
• I assume a communications session once per day, and a 50% duty cycle (i.e., 12 hours / day).
◦ 1 Gigabyte per year requires transmitting 507 bits/sec 12 hours per day.
• 1064 nanometers = 2.818 × 1014 Hz.
◦ A 100 picosecond pulse has a bandwidth of ~10 GHz, or < 0.1 nanometer at 1000 nanometers.
◦ Similarly, full transverse thrust will change the spacecraft's velocity by $<10^{-4}$ c / day, changing wavelengths by < 0.1 nanometer / day.
◦ Conclusion: We can do 1 nanometer wavelength windows if we need to.
◦ I also assume we can support 1 nanosecond time gating if we need to.
◦ To keep the spacecraft simple, I assume 10 nanometer wavelength windows at the spacecraft, and 1 nanometer gating on Earth.

Telescope limits
A 1.26 telescope has a resolution of 33 million km (0.22 AU) from Proxima Centauri
◦ The Sun will at times be in the field of view.
• The Proxima b orbit is 0.04828 AU (7.22 million km) with a period of 11.186 Earth days.
◦ I contend that in practice we shouldn't try and predict where we will be relative to Proxima b 4.24 years in advance, and so the uplink spot size should be & 7 million km.
◦ That implies a maximum uplink telescope size ~6 meters.
◦ Bigger telescopes can (and should) be used for downlinking.
For both up and down links, there is a good chance that the star (Proxima, for downlinks, and the Sun, for downlinks) will be in the field of view.
◦ At 1064 nm, the Proxima flux will be 104,300 photons s^{-1} m^{-2} nm^{-1}
◦ At 1064 nm, the Solar flux will be 4.696 × 107 photons s^{-1} m^{-2} nm^{-1}
• Just using a bigger telescope at the receive end does not help overcome a confusion limited situation.
◦ Ten times the collecting area gives you 10 times as many photons from your spacecraft, but also also get 10 times as many from the star.

• At Earth, for up-linking, this could be brute-forced by increasing the transmit power.
• That option is less desirable 4 light years away. The real solution to the confusion problem is gating.

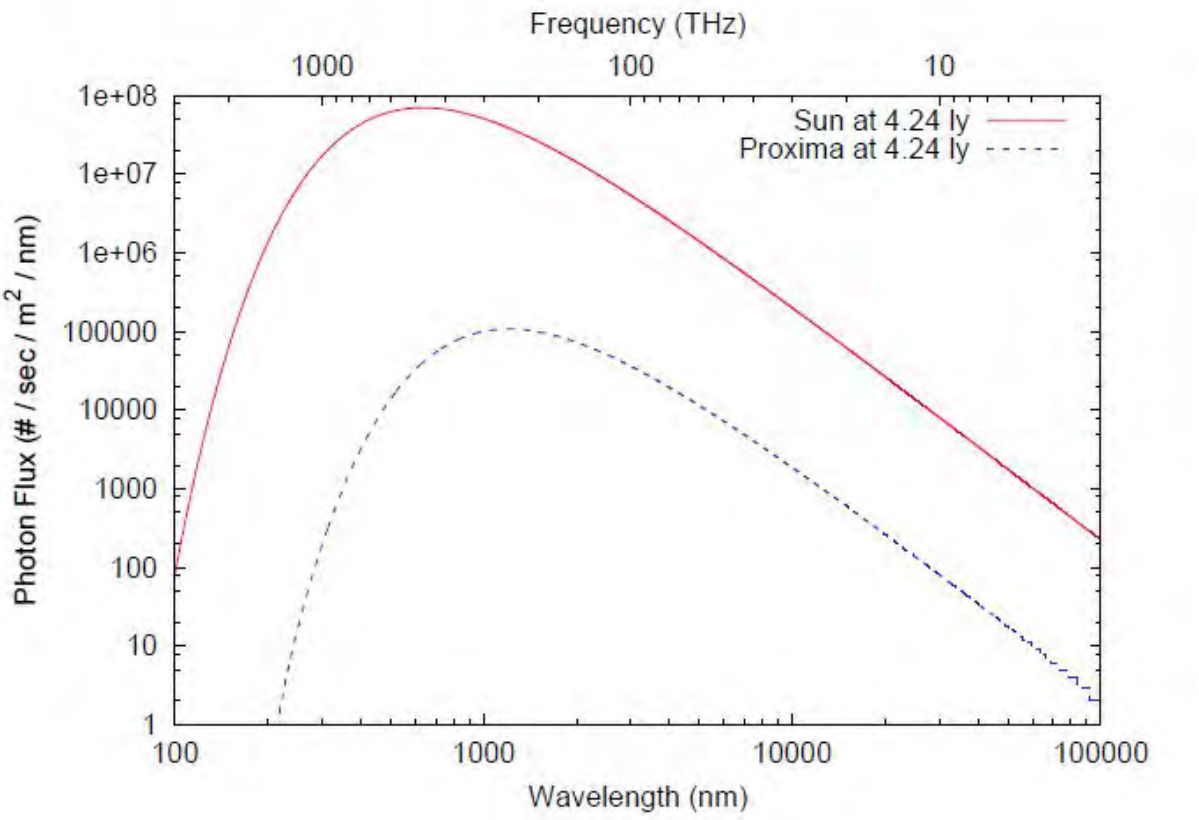

Figure 7.4 Photon flux of a star verses wavelength, at a distance of 4.24 Ly.

In a mission to another star, the spacecraft will typically be angularly close to the target star. This creates confusion limited communications; looking at the spacecraft signal will mean in most cases dealing with the stellar background. Dealing with this stellar interference will be a major design goal.

Assume we are using a 1 kW laser (these are being tested at JPL now).
◦ At 1064 nm, one photon carries 1.867×10^{-19} J.
◦ 1 kW at 1064 nm thus implies 5.356 × 1021 photon / second.
◦ At 4.24 light years a 1.26 m telescope will deliver 6.26 photon m^{-2} s^{-1} back here at Earth.
• A "goodput" of 500 bits / second, at an efficiency of 1 bit/photon implies we need a collecting area of 100 m^2. Let's be conservative and assume a collecting area of 1000 m^2.
◦ That could be 30-meter telescope, an array, etc. In particular, it could be a "photon bucket," such as the 17 meter "MAGIC" Cosmic Ray telescopes [29], which are much cheaper than a similarly sized optical telescope with an optical quality mirror.

Assume that each second is divided into 1024 1-nanosecond time gates (or “bit-bins”), each separated by ∼1 millisecond. Each time gate is also subject to a 1 nm wavelength filter.
◦ Suppose you want to send 1 bit. You could send a pulse for ”1” and no pulse for ”0” but then the power used depends on the data being sent.
◦ It’s better to have 2 slots, a pulse in the first one means ”0” and in the second slot, ”1.” That way, the total power does not depend on the bits being sent.
◦ This is known as optical Pulse Position Modulation (PPM), which has been proposed before for interstellar communications [30]. In this specific proposal, 512 pulses (and thus 512 bits) would be sent per second.

Error Bits

With a 1000 m^2 receiving aperture, each nanosecond duration bit-bin will have an expected value of 0.1 Proxima photons in it, and 6 data photons (if it is receiving a pulse).
• The probabilities here can be modeled by Poisson statistics. Suppose the receive photon gate is set at 2 photons (i.e., 0 or 1 photons in a bit-bin is a miss, more is a hit) and each pulse can go into 1 of 2 bins (so that each pulse encodes 1 bit).
◦ The probability of a Proxima photon causing a false bit to be received is $\sim 4 \times 10^{-3}$ per empty bin.
◦ The probability of not receiving a bit when one is sent is $\sim 1.7 \times 10^{-2}$.
• This sums to a bit error rate of ∼ 11 bit errors per second, or about 2%, which could easily be corrected using error-correction codes.
• The throughput is 1 bit per 6 photons received, which is well below current standards.
• There are certainly better encoding schemes for this problem; my point is to provide an easy to understand method illustrating that useful bit rates can be achieved. I think that in reality we could obtain 3 Kbps or more from Proxima with the system I outlined here.
◦ Or we could deliver 1 Gbyte / year from a distance of 10 light years.

Conclusions

We can achieve useful interstellar laser communication with technology currently being developed.
• The largest mass component for the communications system will be the 1.26 meter telescope. The Kepler space telescope is almost the same size (0.95 meter diameter), has a mass of 478 kg, and is 4.7 m long.
• If the mass of a space telescope scales with the area, our telescope would have a mass of ∼850 kg. If we kept the same f/D, it would be ∼6 meters long.
• Note that many countries could or do possess telescopes or photon buckets capable of receiving transmissions at these levels of photon flux. As there will be no realistic chance to request rebroadcast, a multiplicity of efforts would be beneficial to the project and downlink from Proxima could and probably should be made into an international effort.

7.3 Navigation system on the probe

Three of us HF, TME and JJAR have recently submitted a grant application to study deep space optical navigation (DSON proposal #17-17STP-Prop-0066) in more detail. The idea being that the optical communications system could be dual purpose and also used for navigation if a standard GPS type clock was onboard. Timing signals from 3 or more Earth stationary lasers could be used to triangulate position if the distance out from earth was known, using accelerometers and dead reckoning onboard.

There is also the possibility of using light from known Xray pulsars to triangulate position since their distance apart will change based on the distance of the spacecraft from earth. If the distance from Earth is known (by dead reckoning) we also know how far the pulsars positions would appear to have moved and so we can tell our position by timing pulses arrival times from the pulsars. [31,32]

Whether using laser light or light from pulsars, at relativistic speeds it will be necessary to take relativistic aberration into account. [33]

7.4 Power plant onboard (fission or fusion?)

Reactor Availability 2017: "Small" (10 MWe) modular reactors for space:

https://ntrs.nasa.gov/archive/nasa/casi.ntrs.nasa.gov/20130001608.pdf Heat shield and design.

Find below a summary of the reactor and power conversion subsystems (RPCS) in the Prometheus Jupiter Icy moons orbiter (JIMO)[27] vehicle as defined in the Prometheus Reactor Final report. Please note the maximum length of 9.0m for the fast spectrum reactor, 4 Brayton gas-cycle turbo-alternator version of this RPCS stack. Now that we have the length of the longest 4-turbo-altnerator RPCS, the other required x, y, and z-axis dimensions for the 2-turbo-alternator PCS can be scaled from these drawings. The Prometheus team had settled on the 2-Brayton turbo-alternator 2-2-2 version by the time this project was terminated. This family of RPCS had a preliminary mass estimate of 3,000 to 5,000 kg, which includes the reactor shield in all cases.

The baseline thermal power for this reactor was 1.0 mW-thermal with full power electric output of 200 kWe for 15 years with reduced output to 25 years. Another point that was made clear in this report was that the USA no longer has the capability of testing fast spectrum fission reactors… and that we will have to go to Japan.

The reactor modules are shown below (one for built in redundancy). The reactor instrumentation and control is built into the bus segment.

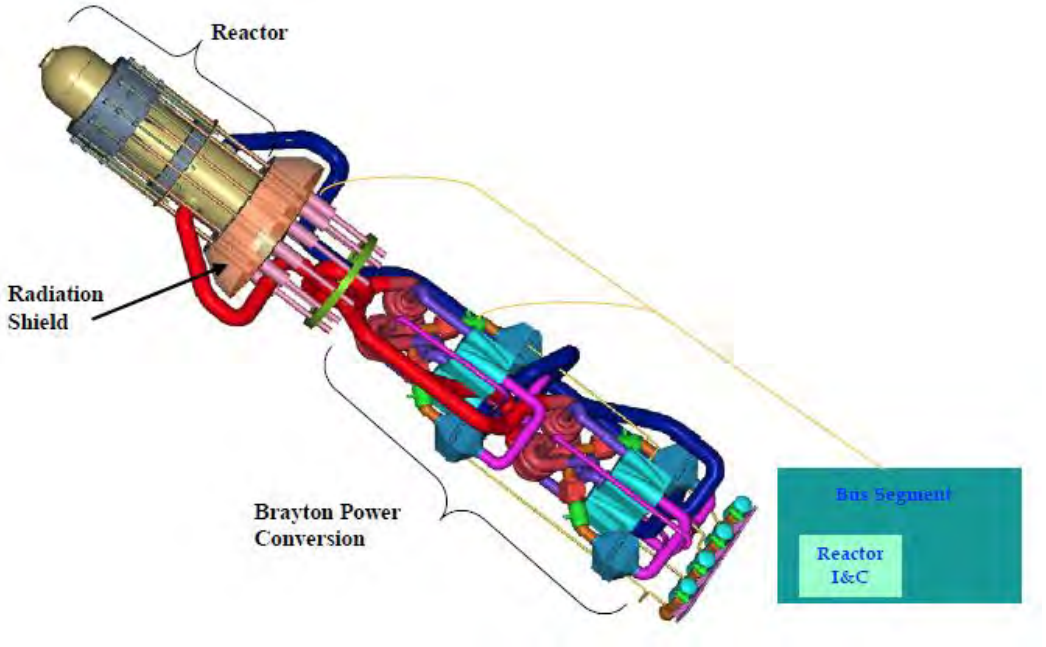

Figure 7.5 Nuclear Reactor with Brayton power conversion from the Prometheus Project JIMO.

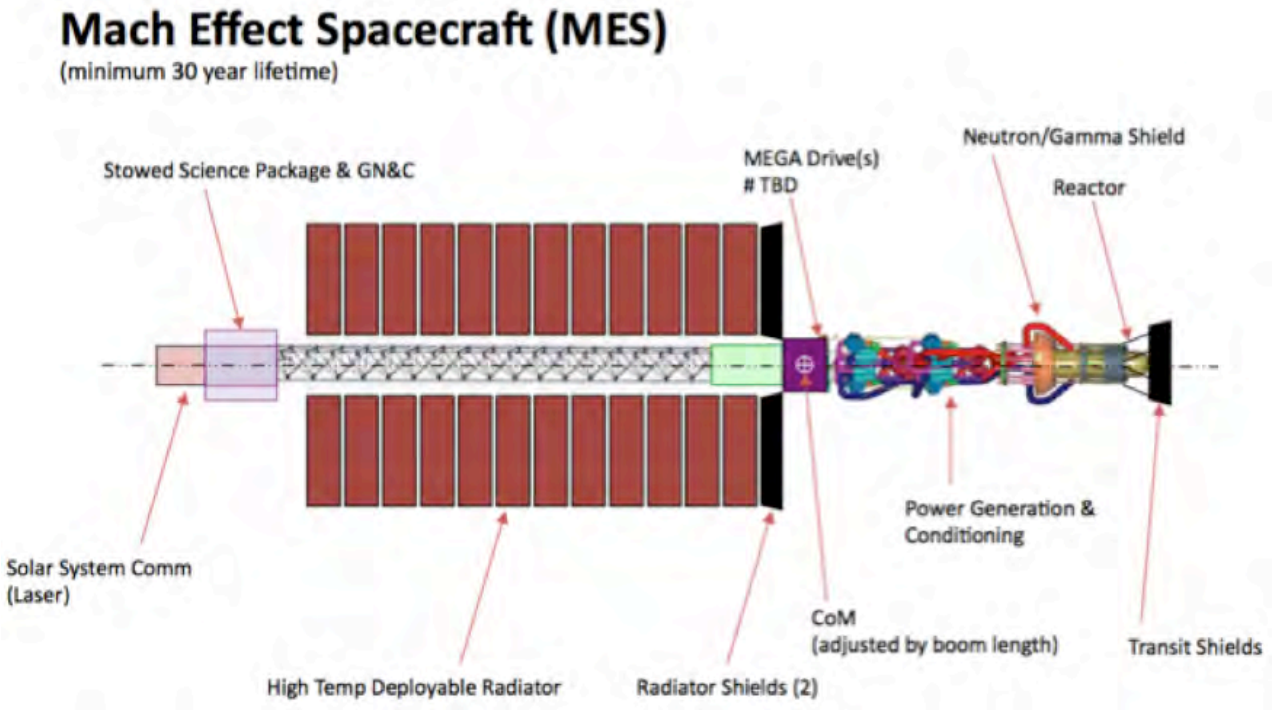

Figure 7.6 Design of the Mach effect spacecraft. Actually we will use 3 radiation shields not two shown here.

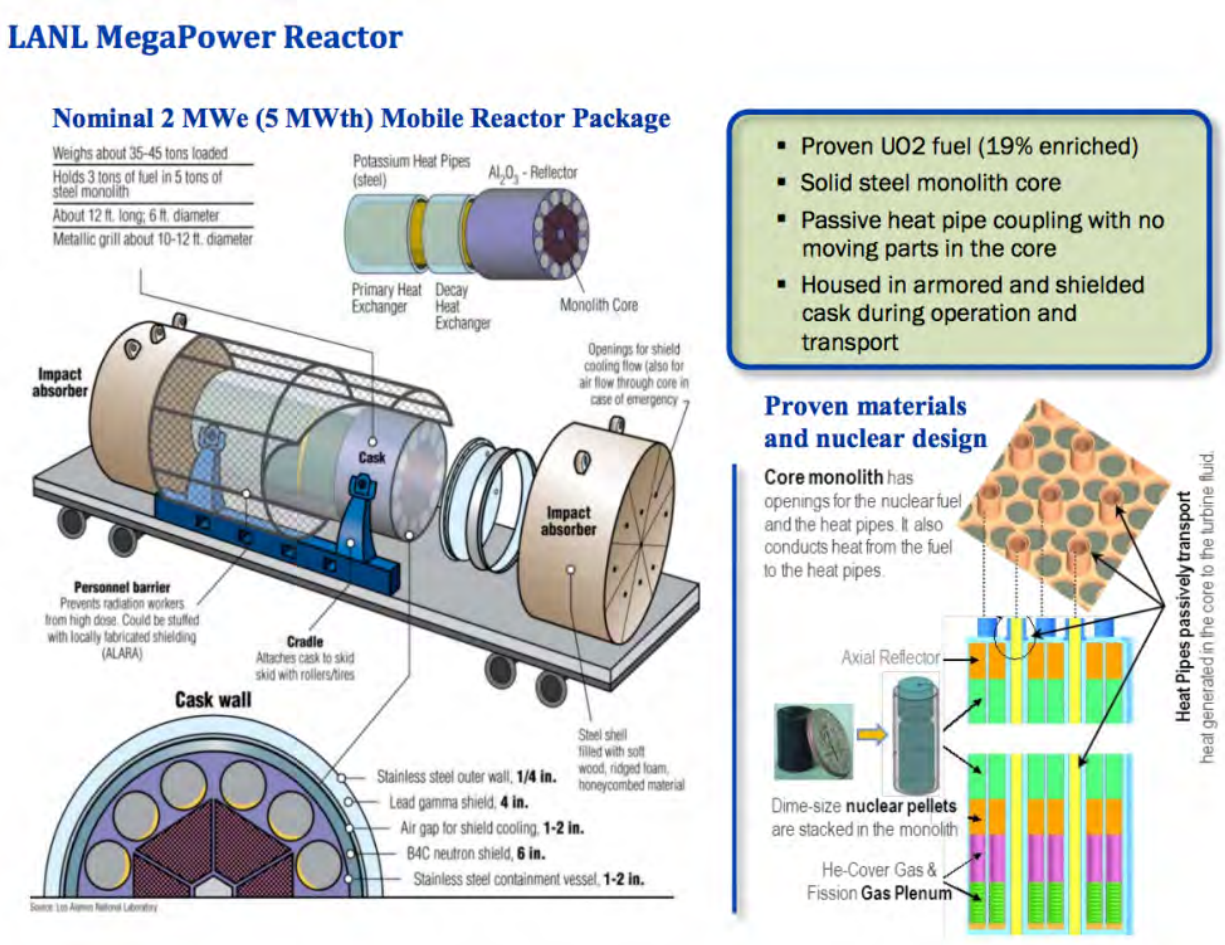

Figure G-1. MegaPower Reactor Systems

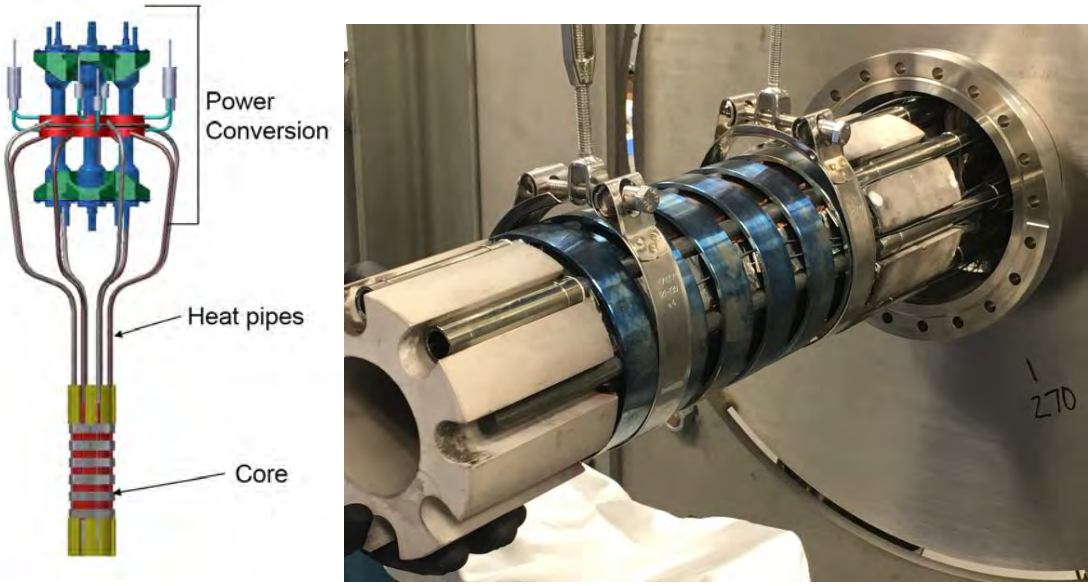

Figure 7.7 https://www.nextbigfuture.com/2017/07/very-small-modular-nuclear-fission-reactors-for-military-and-space-applications.html

8. S.W.A.T. Analysis

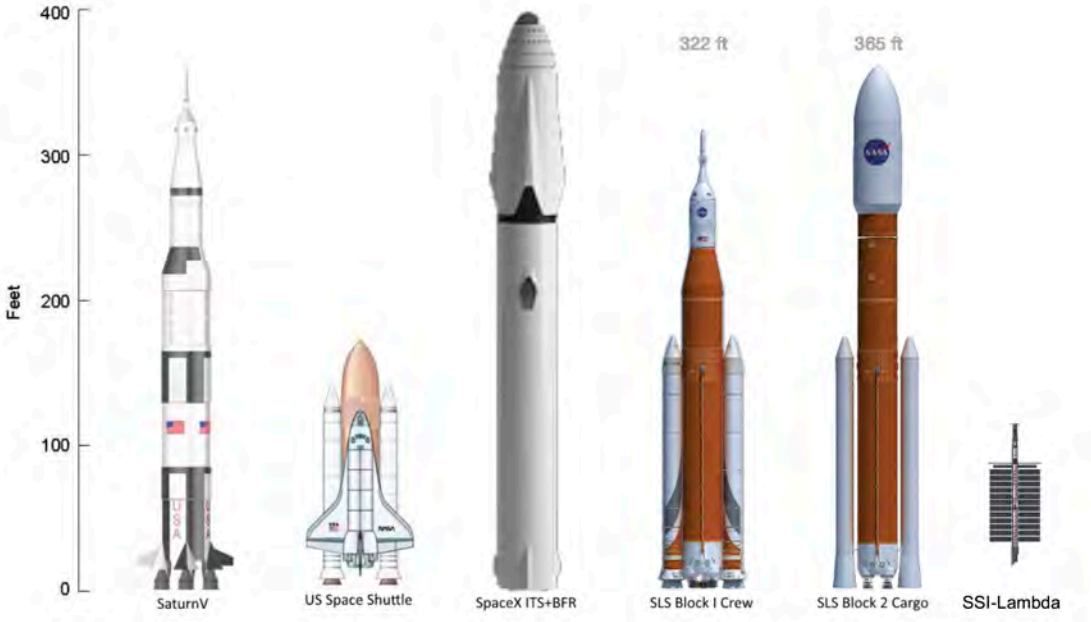

Figure 8.1 Size of the probe compared with other spacecraft.

Size:
The probe is approximately 75 feet long. It is shown here compared with other spacecraft, and is roughly the same length as the space shuttle.

Weight
The weight of the probe is ~15,000 kg. This is mostly shielding and heat radiators which could be reduced with the use of a fusion reactor.

Power
The probe power requirements are 5MW-thermal or 1.5MW-electric fission reactor, which may become available within a 20 year time frame, see Figure 1.1 on p4. This would supply 1500, 1kW MEGA drives and the scientific equipment onboard. Not all the MEGA drives need to be running at once.

9. S.W.O.T. Analysis

Strengths

The SSI-Lambda probe using MEGA drive thrusters is a truly propellantless-propulsion space craft. It can travel at speeds up to the speed of light in a vacuum c with only consumption of electric power. It allows for one of a kind interstellar missions with breaking into the target system. It can revolutionize space travel and also lead to many benefits for heavy lift here on Earth.

Weaknesses

The MEGA drive so far has not been tested in space. The drives have also not been tested for long time durations (years) which will be necessary for interstellar missions. There is the possibility of depolarization of the materials and other breakdown mechanisms. The MEGA drive requires further development for heavy lift capability.

Opportunities

The probe allows for rapid transit times to distant solar system planets and interstellar travel. No other method for travelling to the stars and breaking into the target system has been put forward to date, which also has credible physics to back it up. The ability to break into the target system will allow years of exo-planet study rather than a few days in a fly-by mission. The possibility of taking landers and dropping smaller probes into the atmosphere of an exo-planet exists.

Threats

Will it be possible to increase the thrust of the MEGA drives by using new materials, or higher voltage, or higher frequency by changing the dimensions of the device? Will using arrays of devices increase the thrust linearly or will some acoustic interference decrease the effect? Will self healing materials become available to avoid the problems of shakedown, depolarization and cracking? There are many unknowns which require further study. The theory is extremely complex and requires extensive modeling and simulation. No replications have been made at tier 1 universities in peer review journals.

10. Conclusions and Recommendations

The current devices are producing a small thrust of a few micronewtons. This is not sufficient for interstellar travel applications. However, the physics seems credible and worth pursuit. We recommend further testing. The benefits outweigh the costs of a replication at a tier 1 university and testing new materials and arrays of devices. The main emphasis on future work should be to increase the thrust of each device.

11. References

[1] Slide on fission reactors of the future, by Lee Mason at NASA Glen Research Center.

[2] Fusion reactor, Dr. Stephanie J. Thomas, Princeton Satellite Systems NIAC phase II 2017.

[3] Fusion reactor, Dr. Raymond J. Segwick, University of Maryland, NIAC phase I, 2017.

[4] H. Fearn & L. L. Williams editors, "Proceedings of the Estes Park Advanced Propulsion Workshop", Estes Park CO , September 19-22 (2016). Free download is available at the Space Studies Institute (SSI.org) http://www.ssi.org

[5] J. F. Woodward, "Making Starships and Stargates, The science of Interstellar Transport and Absurdly Benign Wormholes", Springer Press, New York, December 2013.

[6] I. A. Ciufolini & J. A. Wheeler, "Gravitation and Inertia", Princeton Series in Physics, Princeton University Press, New Jersey (1995).

[7] C. H. Misner, K. S. Thorne & J. A. Wheeler, "Gravitation", W. H. Freeman and Company, San Francisco 1973.

[8] J. B. Barbour & H. Pfister editors, "Mach's Principle: From Newton's Bucket to Quantum Gravity", Birkäuser , Berlin (1995).

[9] K. Wanser, "Center of mass acceleration of an isolated system of two particles with time variable masses interacting with each other via Newton's third law internal forces: Mach effect thrust 1", Journal of Space Exploration 2, (2) pp121-130 (2013).

[10] F. Hoyle and J. V. Narlikar, "Action at a distance in physics and cosmology", W. H. Freeman & Company San Francisco (1974). See also, Hoyle, F. and Narlikar, J.V. (1964) *Proceedings of the Royal Society of London A*, **282**, 191. http://dx.doi.org/10.1098/rspa.1964.0227 and Hoyle, F. and Narlikar, J.V. (1966) *Proceedings of the Royal Society of London A*, **294**, 138. http://dx.doi.org/10.1098/rspa.1966.0199

[11] Sean M. Carroll, "Spacetime and Geometry", Pearson Education Ltd. (2013) p281.

[12] Steven Weinberg, "Gravitation and Cosmology Principles and Applications of the General Theory of Relativity", John Wiley & Sons, New York (1972).

[13] H. Fearn, et al. "Mach effect gravity assist drive", presented at the Foundations of Interstellar Studies Workshop, at City Tech, CUNY, June 13-15, New York (2017). To be published in JBIS.

[14] *Advanced Propulsion workshop* held at Aerospace Cooperation, El Segundo, November 1-3, 2017. Proceedings to be published by JBIS and videos on ssi.org.

[15] Steiner and Martins piezoelectrics CO. https://www.steminc.com/ material properties https://www.steminc.com/PZT/en/piezo-materials-properties

[16] APC International Ltd, , Piezoelectrics Ceramics & Piezo components, https://www.americanpiezo.com/
the material properties can be found here; https://www.americanpiezo.com/apc-materials/physical-piezoelectric-properties.html

[17] Tong-Yi Zhang et al., "Failure behavior and failure criterion of conductive cracks (deep notches) in thermally depoled PZT-4 ceramics", Acta Materialia , 51, pp4881-4895 (2003).

[18] José Rodal, private communication new model. See also, "A Machian wave effect in conformal scalar-tensor gravitational theory", under peer review since Oct 13, 2017. Astrophysics and space science, Springer.

[19] Fujifilm Prescale. Pressure Metrics LLC, www.pressuremetrics.com Medium (MS) film.

[20] K. L. Johnson, "Contact Mechanics", Cambridge University Press, 1985. (See Rigid punch pp35-38. Also Eq. (2.24b) using Log[s-x] for $x \leq$ a where a is the radius of the disc.)

[21] Ian N. Sneddon, "The relaxation between load and penetration in the axisymmetric Boussinesq problem for a punch of arbitrary profile", Int. J. Engineering Sci. 3, pp47-57 (1965).

[22] J. R. Barber, "Indentation of an elastic half-space by a cooled flat punch", http://qjmam.oxfordjournals.org/ Radcliffe science library.

[23] S. G. Turyshev, Wave-theoretical description of the solar gravitational lens, Phys. Rev. D 95 (8) (2017) 084041. arXiv:1703.05783, doi:10.1103/PhysRevD.95.084041.

[24] L. A. Alkalai, N. A. Arora, S. T. Turyshev, M. S. Shao, L. F. Friedman, Solar Gravity Lens Team, Mission to the Solar Gravity Lens Focus: Natural High-Ground for Imaging Earth-Like Exoplanets, in: Planetary Science Vision 2050 Workshop, Vol. 1989 of LPI Contributions, 2017, p. 8203.

[25] Andreas M. Hein, T. M. Eubanks et al. "Project Lyra: Sending a Spacecraft to 1I/'Oumuamua (former A/2017 U1), the Interstellar Asteroid", arXiv: physics.space-ph 1711.03155

[26] T. M. Eubanks, Invited article for Principium, the community magazine of the Initiative for Interstellar Studies. "Preparing for the next Interstellar Object", https://i4is.org/publications/principium/

[27] Prometheus JIMO Final Report. https://ntrs.nasa.gov/search.jsp?R=20060043352
large.stanford.edu/courses/2017/ph241/mangram2/docs/982-R120461.pdf

[28] D. M. Boroson and B. S. Robinson. The Lunar Laser Communication Demonstration: NASA's First Step Toward Very High Data Rate Support of Science and Exploration Missions. Space Science Reviews, 185:115–128, Dec. 2014. doi: 10.1007/s11214-014-0122-y.

[29] J. Aleksi´c and the MAGIC Collaboration. The major upgrade of the MAGIC telescopes, Part I: The hardware improvements and the commissioning of the system. Astroparticle Physics, 72: 61–75, Jan. 2016. doi: 10.1016/j.astropartphys.2015.04.004.

[30] M. Ross. Large M-ary pulse position modulation and photon buckets for effective interstellar communications. In S. A. Kingsley, editor, The Search for Extraterrestrial Intelligence (SETI) in the Optical Spectrum, volume 1867 of Proc. SPIE, pages 161–177, Aug. 1993

[31] W. Becker, M. G. Bernhardt and A. Jessner, " Autonomous Spacecraft Navigation with Pulsars", arXiv: 1305.4842

[32] L. M. B. Winternitz et al. " Xray Pulsar Navigation Algorithms and Testbed for SEXTANT", http://ieeexplore.ieee.org/stamp/stamp.jsp?arnumber=7118936

[33] E. Calabro, "Relativistic aberrational interstellar navigation", Acta Astronautica 69 (2011) pp360-364.

Appendix A: Circuit upgrades feedback/control

Circuits for the Mach effect experimental lab. We need an impedance matcher for the single and second harmonic frequencies.

Below are the schematics for the impedance matcher build by Bruce Long. Because of the need to maximize the resonant power transfer from the lab's ac power supplies to the MEGA-drive test articles needed to maximize thrust output, Dr. Long volunteered to design and build an impedance matching box that could handle two drive channels with one being for the MEGA-drive's 1-omega drive frequency over a frequency range of 20 kHz to 120 kHz with the nominal design frequency being 36.0 kHz,. The second channel is required to drive the 2-omega force rectification signal over a frequency range of 40 kHz up to 240 kHz with its nominal design frequency being 72.0 kHz.

The source output impedance of the CSUF lab amplifiers that are used to drive this impedance matching unit vary from a low of 2.0 ohms (Bridged Carvin Amps) up to a high of 50 ohms, while the MEGA-drive test-article's input impedances for each channel, which are primarily capacitive in nature, vary per the Xc = 1/(2*Pi()*f*c) capacitive reactance equation, where f is the drive frequency in Hz and c is the PZT Stack's capacitance in Farads measured at the drive frequency. The impedance box's chosen MEGA-drive test article's capacitance range has to accommodate a capacitance range from ~5.0nF up to ~50.0nF. This implies that the load's capacitance reactance range can be from **~1,591 ohms** for a 5.0nF load at 20.0 kHz case, and **13.26 ohms** for the 50.0nF at 240.0 kHz case. Thus the impedance matching unit has to accommodate an input to output impedance range of up to 1,591/2.0 = ~796X, which obviously can't be supplied with a fixed tuning circuit.

To accommodate this large impedance ratio, Dr. Long chose to provide a manual impedance tuning configuration for each the of 1w and 2w drive channels that consist of a transformer isolated input for each channel, with a primary to secondary winding 1 to ~3 step-up turns ratio or a 1-to-9 impedance ratio. The rest of the impedance matching devices in each impedance matching channel consist of a large variable roller inductor with additional discrete inductor and capacitive components that can be switched in and out of each channel's circuit while observing the ac output voltage and current waveforms from the impedance matching box going to the test article in question. The goal for this type of resonant tuning is to find the best tuning solution that maximizes both the peak voltage and current for a given test article's 1w and 2w signals at their respective drive frequencies, while also obtaining the desired phase relationship between the two. (The MEGA-drive's thrust is maximized when the phase between the 1w drive voltage and the 2w drive current is 90 degrees leading or lagging the 1w reference voltage waveform. The sign of this phase difference determines the direction of the thrust.)

This impedance matching unit was built, tested and delivered to the CSUF MEGA-Drive laboratory in November 2017.

Design Drive Frequencies 1F= 36kHz, 2F=72kHz
Cdut = 18nF
Cdut reactance at 1F = -j246 at 2F = -j123

Design Procedure

Design 1F path first
Design 2F block parallel resonant circuit

Let C12= Cdut = 18nF, Find L12

72kHz = 1/(2 pi root(L12 * 18 nF)

L12 = 272 uH

Find reactance of L12 in parallel with C12 at F1
At F1 L12 = +j61.4, C12 = -j246

$$L12::C12 = \frac{1}{\frac{1}{+j61.4} + \frac{1}{-j246}} = +j81.8$$

Select L11 so that L11 + (L12::C12) + Cdut are series resonant

:xL11: + x:L12::C12: + :xCdut: = 0

:xL11: + j81.8 + -j246 = 0

:xL11:= +j164 at 36 kHz

L11= 725uH

- -

Design 2F path
Design 1F block parallel resonant circuit

Let C22= 4* Cdut = 72nF, Find L22

36kHz = 1/(2 pi root(L22 * 72 nF)

L22 = 272uH

Find reactance of L22 in parallel with C22 at F2
At 2F L22 = +j123, C22 = -j30.7

$$x(L22::C12) = \frac{1}{\frac{1}{+j123} + \frac{1}{-j30.7}} = -j40.9$$

Select L21 so that L21 + (L22::C22) + Cdut are series resonant

:xL21: + x:L22::C22: + :xCdut: = 0

:xL21: + - j40.9 + -j123 = 0

:xL21:= +j163 at 72 kHz

L21=360uH

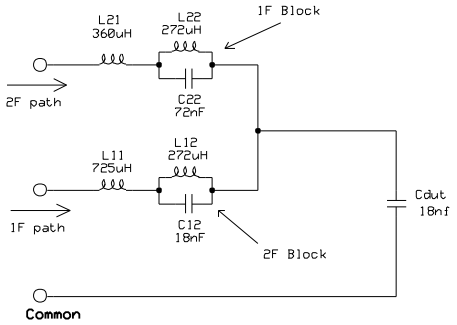

Drawing made with Expresspcb schematic capture app
Original .sch file available upon request

Dual resonant matching network		
Cdut=18nF, 1F=36kHz, 2F=72kHz		
Bruce Long	Rev 1.0 5/26/2016	Sheet 1/3

Component	Value	Reactance 1F	Reactance 2F
L11	725uH	+j164	+j328
L12	272uH	+j61.5	+j123
C12	18nF	-j246	-j123

Component	Value	Reactance 1F	Reactance 2F
L21	360uH	+j81.4	+j163
L22	272uH	+j61.5	+j123
C22	72nF	-j61.5	-j30.75
Cdut	18nF	-j246	-j123

Equivalent circuit at 1F 36kHz

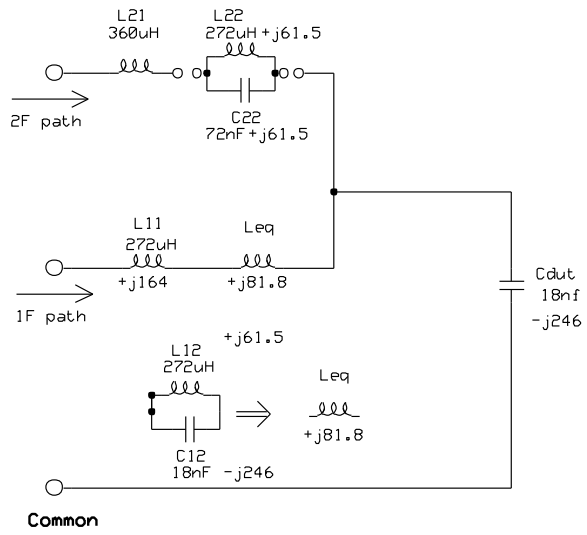

Equivalent circuit at 1F 36kHz

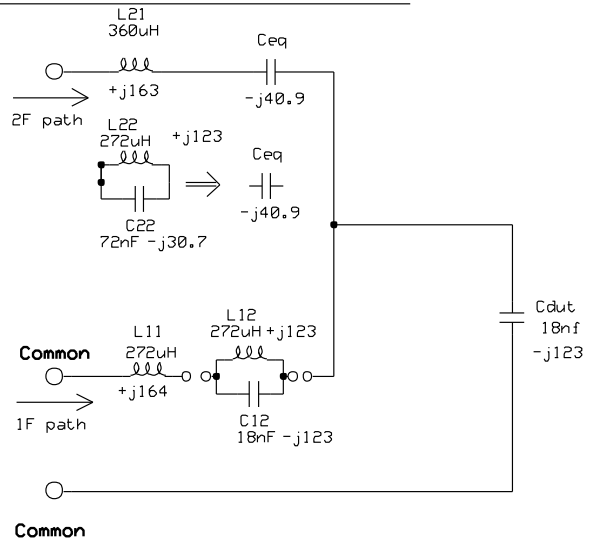

Drawing made with Expresspcb schematic capture app
Original .sch file available upon request

Dual resonant matching network		
Cdut=18nF, 1F=36kHz, 2F=72kHz		
Bruce Long	Rev 1.0 5/26/2016	Sheet 2/3

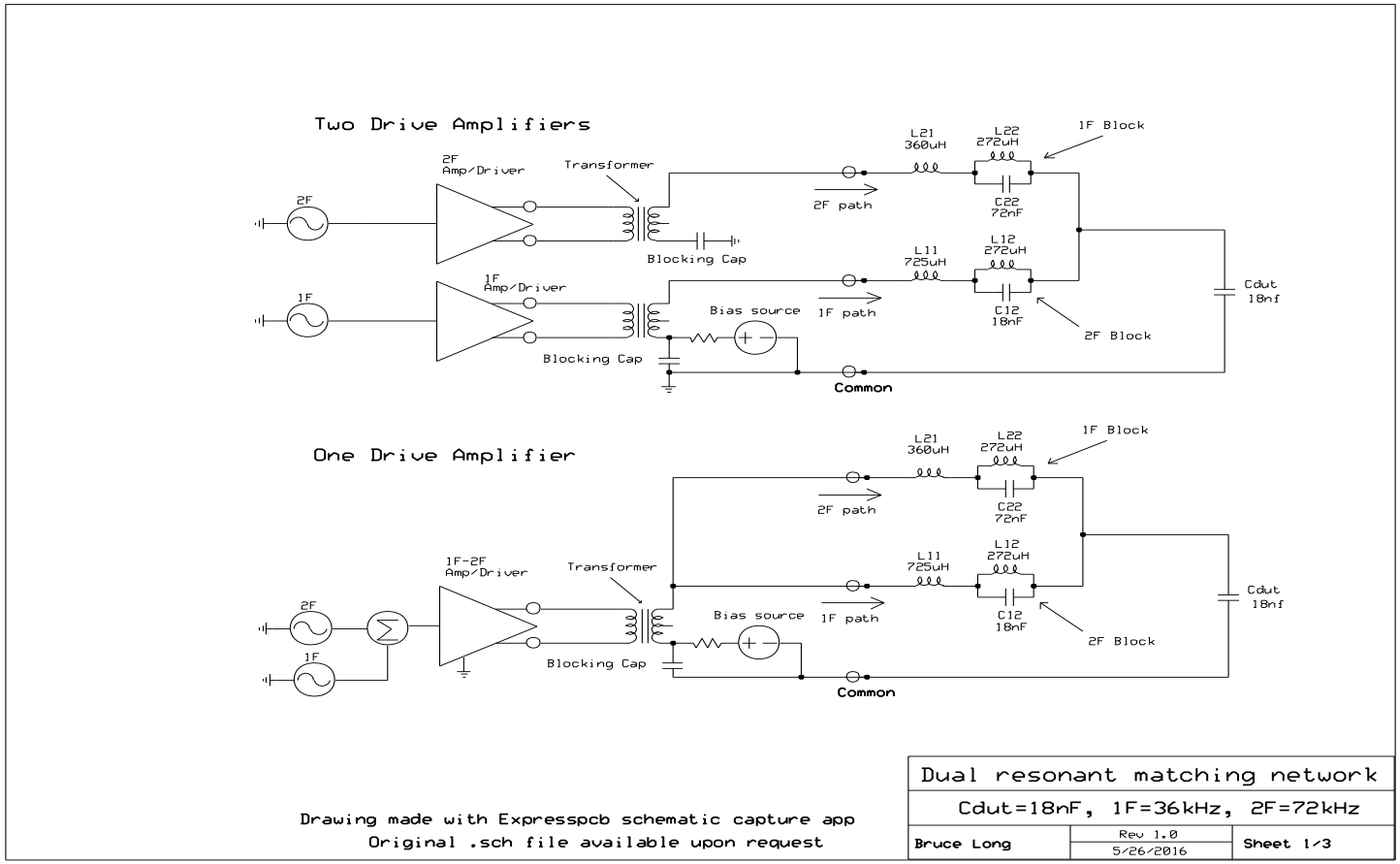
Two Drive Amplifiers
2F
Amp/Driver
Transformer
2F
L21
360uH
L22
272uH
1F Block
2F path
C22
72nF
Blocking Cap
L11
725uH
L12
272uH
1F
Amp/Driver
Cdut
18nf
Bias source
1F path
C12
18nF
1F
2F Block
Blocking Cap
Common
One Drive Amplifier
L21
360uH
L22
272uH
1F Block
2F path
C22
72nF
1F-2F
Amp/Driver
Transformer
L11
725uH
L12
272uH
2F
Cdut
18nf
Bias source
1F path
C12
18nF
1F
2F Block
Blocking Cap
Common
Drawing made with Expresspcb schematic capture app
Original .sch file available upon request
Dual resonant matching network
Cdut=18nF, 1F=36kHz, 2F=72kHz
Bruce Long
Rev 1.0
5/26/2016
Sheet 1/3

The following modifications were proposed by Paul March. His circuit was checked using CircuitMaker software seen below.

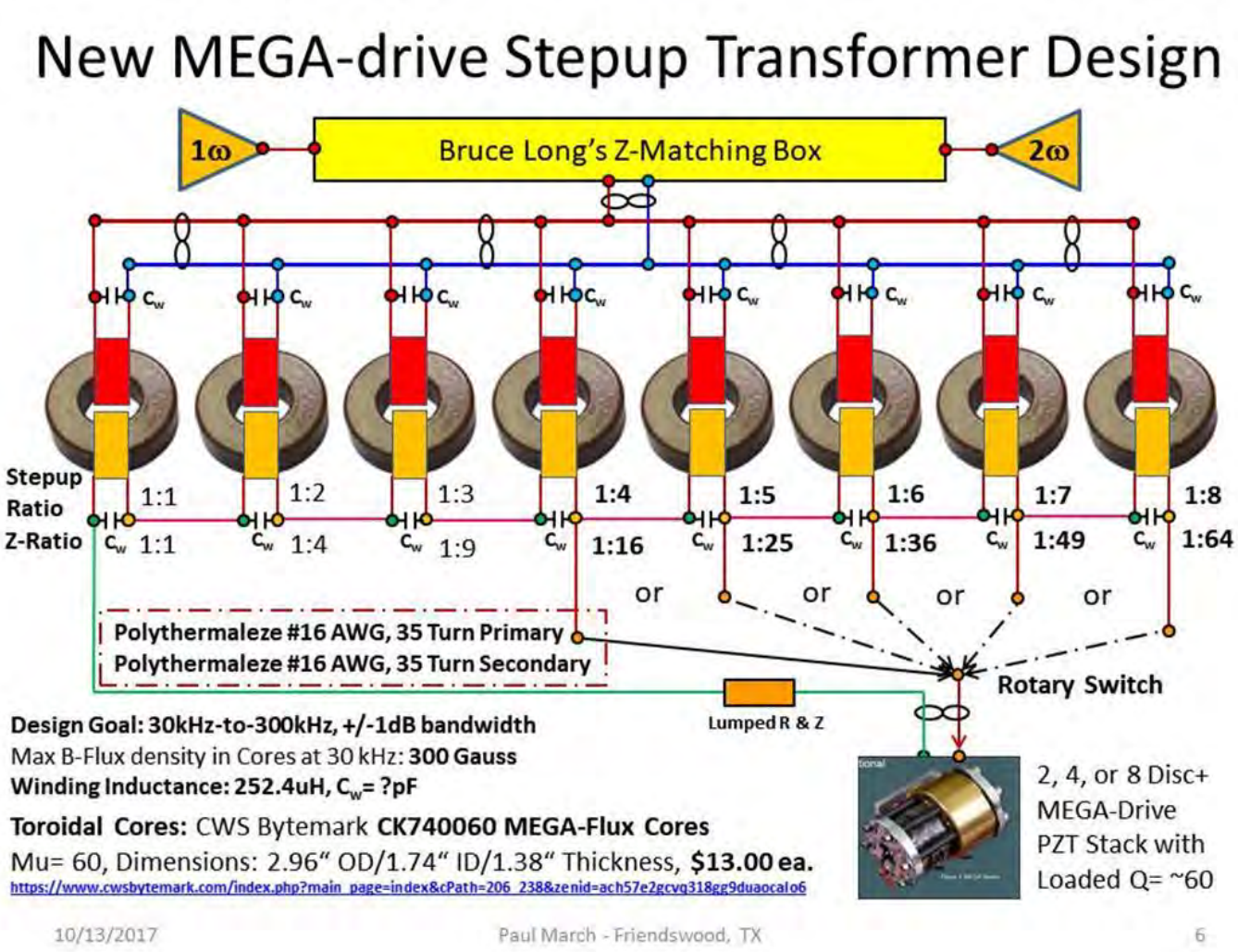

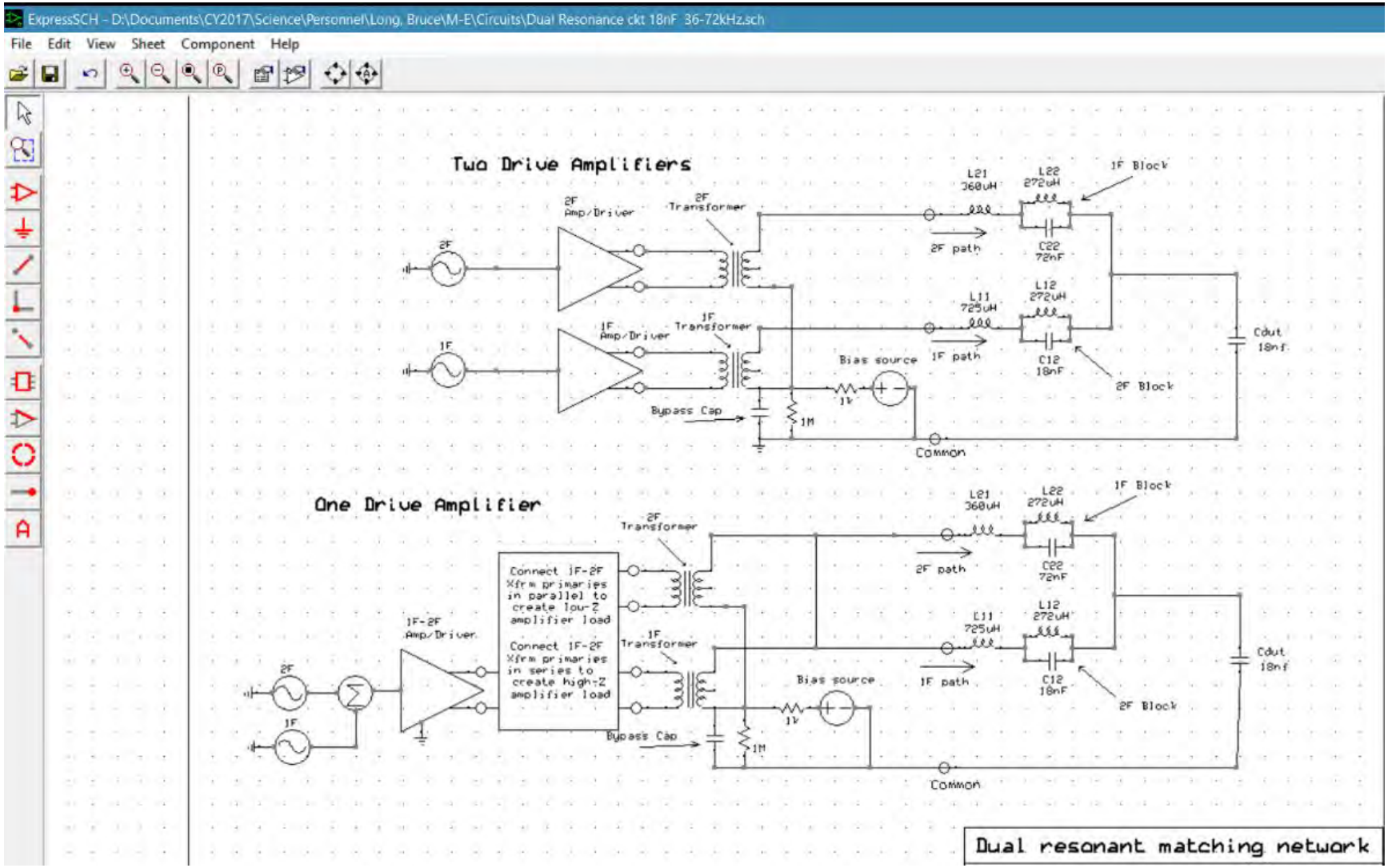
ExpressSCH - D:\Documents\CY2017\Science\Personnel\Long, Bruce\M-E\Circuits\Dual Resonance ckt 18nF 36-72kHz.sch
File Edit View Sheet Component Help
Two Drive Amplifiers
2F Amp/Driver
2F Transformer
2F
1F
1F Amp/Driver
1F Transformer
Bias source
1k
1M
Bypass Cap
Common
L21 360uH
L22 272uH
C22 72nF
L11 725uH
L12 272uH
C12 18nF
Cout 18nf
2F path
1F path
1F Block
2F Block
One Drive Amplifier
1F-2F Amp/Driver
Connect 1F-2F Xfrm primaries in parallel to create low-Z amplifier load
Connect 1F-2F Xfrm primaries in series to create high-Z amplifier load
Dual resonant matching network

Mach Effects For In-Space Propulsion

Contacts:
H. Fearn hfearn@fullerton.edu
J.J.A. Rodal jrodal@alum.mit.edu
T. M. Eubanks tme@asteroidinitiatives.com

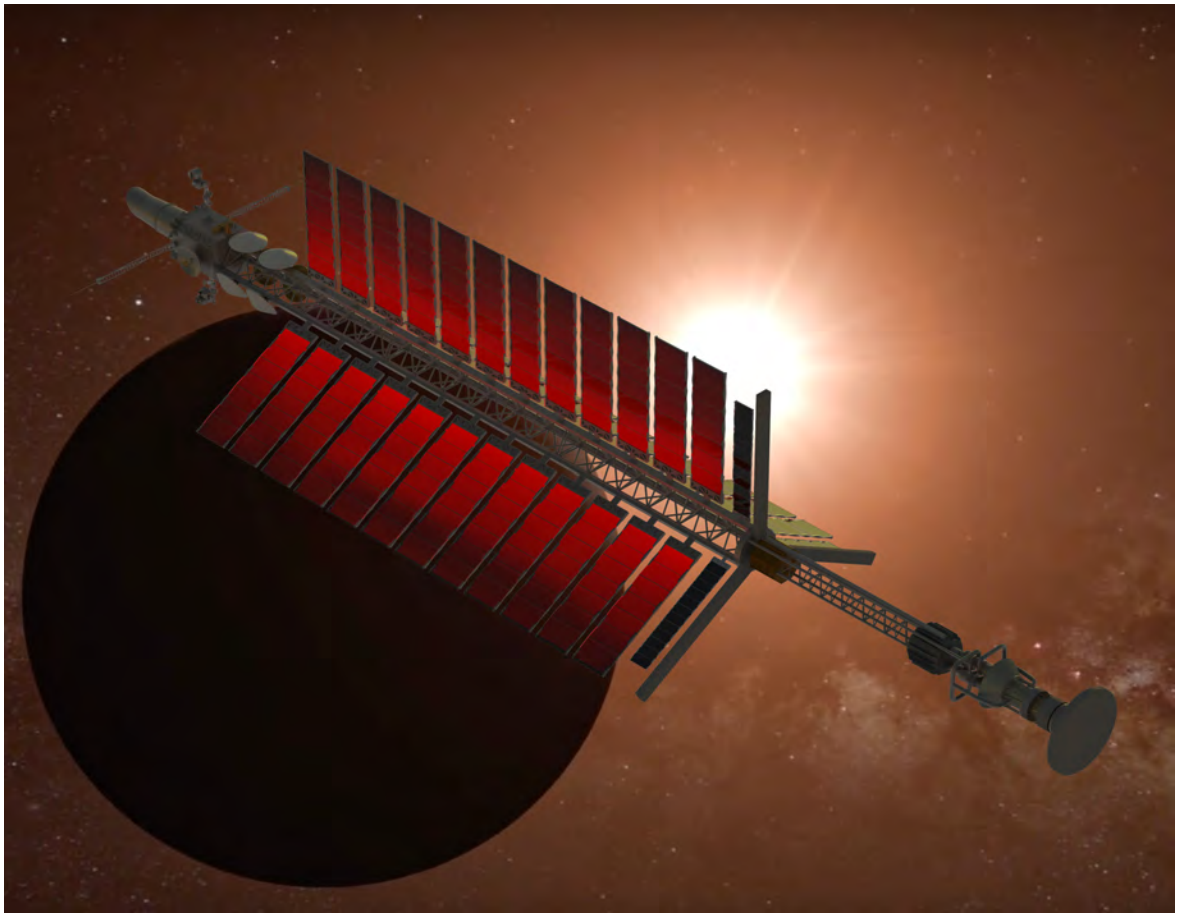

MEGA Drive Q & A:

Q1. Does the MEGA drive actually change mass, and if so, how much?

In our experiments using a device with an initial mass of 0.2 kg, the mass is calculated to fluctuate sinusoidally, at a frequency exceeding 30 kHz, with a zero to peak amplitude on the order of a Planck mass (the mass of a hypothetical black hole whose Schwarzschild radius equals the Planck length). This is a mass fluctuation per unit mass on the order of $\Delta m/m = 10^{-8}$.

The theoretical mass fluctuation is $\Delta m(t) = (1/(4\,\pi\,G\,\rho\,c^2))\,\partial^2 E/\partial\, t^2$, where:

G= gravitational constant= $6.67408 \times 10^{-11}\ m^3/(kg\ s^2)$

ρ = mass density (kg/m^3)

c = speed of light in vacuum = 2.99792458×10^8 m / s

A mass fluctuation per unit mass on the order of 10^{-8} with a period of microseconds is a small variation in mass per unit time. It deserves further experimental and theoretical study. For comparison, here are some more commonly known mass changes:

(1) Combustion: decrease in mass due to combustion of methane in the gas burner of a kitchen stove: $\Delta m/m = -10^{-10}$

(2) Change of phase: increase in mass due to melting of ice: $\Delta m/m = 3.7\text{x}10^{-12}$

(3) Temperature change: increase in mass due to temperature increase of a flat iron by 200 K: $\Delta m/m = 10^{-12}$

(4) Emission of solar power from our Sun: the rate at which the Sun emits energy from its surface (its luminosity), is around 3.8×10^{26} Watts, therefore the rate at which solar mass disappears is=$4.2\text{x}\ 10^9$ kilograms per second. Since the total mass of the Sun is 2×10^{30} kilograms, the change in mass of our Sun per 100 years is $\Delta m/m = 6.5\text{x}10^{-12}$

(5) Strong nuclear force: due to the strong nuclear force, energy is required to separate a stable nucleus into its constituent protons and neutrons. The more stable the nucleus is, the greater is the amount of energy needed to break it apart (called the binding energy of the nucleus). For example, for deuterium (a stable isotope of hydrogen: the bound state of a proton and a neutron), the binding energy and hence the defect of mass is 2.2 MeV, so that $\Delta m/m = 10^{-3}$

Q2. How does the MEGA drive move?

The minimum model of complexity to illustrate the acceleration of the center of mass (X_{COM}) due to variable mass is a system of two masses m_1 and m_2 coupled by a spring k.

$$X_{COM} = \frac{\frac{m_1 x_1}{\sqrt{1 - \dot{x}_1^2/c^2}} + \frac{m_2 x_2}{\sqrt{1 - \dot{x}_2^2/c^2}}}{\frac{m_1}{\sqrt{1 - \dot{x}_1^2/c^2}} + \frac{m_2}{\sqrt{1 - \dot{x}_2^2/c^2}}}$$

A dashpot is also necessary for realistic modeling of the amplitude of vibration, but for simplicity, the acceleration of the center of mass can be demonstrated without a damper. For this illustrative purposes the following assumptions are made:

(1) no damping
(2) very weak gravitational field
(3) uniform gravitational field with respect to the dimensions of the drive
(4) small spin and spin rates
(5) small strain

The positions of the masses from an arbitrary reference point are x_1 and x_2. Time differentiation is shown by the number of overdots (single overdot for the first derivative, etc.). Then, it can be shown that the acceleration of the center of mass ($\ddot{X}_{COM}$) is given by the first time derivative and the second time derivative of the variable masses as follows:

$$\ddot{X}_{COM} = \frac{\frac{2\,\dot{m}_1 \dot{x}_1 + \ddot{m}_1 x_1}{\sqrt{1 - \dot{x}_1^2/c^2}} + \frac{2\dot{m}_2 \dot{x}_2 + \ddot{m}_2 x_2}{\sqrt{1 - \dot{x}_2^2/c^2}}}{\frac{m_1}{\sqrt{1 - \dot{x}_1^2/c^2}} + \frac{m_2}{\sqrt{1 - \dot{x}_2^2/c^2}}} + \text{higher order terms}$$

Notice that:

(1) if the masses are constant, then the acceleration of the center of mass is zero

(2) if the masses are variable but equal, such that m_1=m_2, then the displacements, velocities and accelerations, due to oscillation of the masses at the natural frequency, (in reality the first eigenmode) are equal in magnitude but opposite in sign, and therefore the acceleration of the center of mass is zero.

(3) to accelerate the center of mass it is needed to excite oscillations of unequal variable masses, their rates of change and their displacements and velocities, at two frequencies ω_1 and ω_2, with ω_2=2 ω_1. Multiplication of harmonic terms (the first time derivative of the mass times the velocity and the second time derivative of the mass

times the displacement all being harmonic functions of time) results in even terms having a non-zero time cycle average, for example: $\cos^2(\omega t) = ½ + \cos(2\omega t)/2$. Conservation of momentum for a system of unequal masses with such a fluctuation in mass demands that the center of mass must accelerate.

Q3. Why hasn't this force shown up in experiments up to now?

The force measured by experiment is due to both the piezoelectric and electrostriction effects. Piezoelecticity is only found in certain crystals in nature and is represented by a 3rd order tensor which is uncommon. There are two excitations involved the lowest at around 30kHz and the second at twice that frequency, which is not a common occurrence. The force measured in the current experiments is very small, microNewtons, and would be unlikely to be observed in work that was not focused on anomalous accelerations and anomalous forces.

One possible explanation, left to explore, is that the force maybe hidden by a chameleon field. A chameleon field is a massive scalar field (a "fifth force") following a Klein-Gordon equation with a field mass (and thus a group velocity and Compton wavelength) that depends on the local matter density. The chameleon field would have a Compton wavelength of order 0.1 mm or less in high density regions (such as within the Earth's atmosphere), enabling the theory to survive fifth force tests, but a much lower mass (and larger Compton wavelength) in the vacuum of space. In this theory, the chameleon field in a high-density region surrounded by a vacuum, is confined to a thin screen of order 1 micrometer in depth and thus with a high field gradient, on the surface of the massive body. The group velocity of the field in the various proposed theories would be 100's of meters per second on the surface of a massive body, and very close to the speed of light in deep space.

The test units in our experimental work, in the near vacuum of a test chamber, would have a thin screen and would be vibrating that screen at roughly the frequency (~ v group / R) of the first normal mode of chameleon radiation for the drive stack. These units should thus be efficient radiators of chameleon field radiation, converting acoustic oscillations to chameleon waves in a fashion analogous to how magnetoelectric antennas convert acoustic waves to electromagnetic waves. This chameleon radiation, with its low group velocity at the surface of the body, would carry away substantially more momentum per unit energy than would a photon rocket. (The wave frequency would substantially increase outside of the drive unit, but that does not change the momentum loss at the drive surface). This momentum change will cause a thrust, which should be even larger in deep space than in a vacuum chamber. In a confined vacuum chamber, it would be reasonable

to expect standing chameleon waves to be set up inside the chamber, which may be detectable experimentally.

A literature search does not reveal any other search for fifth force or analogous effects at frequencies much larger than diurnal, roughly 9 orders of magnitude smaller than the 35 kHz used in our experimental work.

There is a lot of theoretical work as well as a few proposed experiments in this area (one of them is a 2017 Phase I NIAC grant by Dr. Nan Yu at JPL, "A direct probe of dark energy interactions with a solar system laboratory").

https://www.nasa.gov/directorates/spacetech/niac/2017_Phase_I_Phase_II/Dark_energy_interactions_solar_system_laboratory

Q4 Doesn't the explanation of Mach's Principle require information to propagate at greater than the speed of light if there is connection between local mass and the distant stars?

If the energy of stars 10^8 light years away were being fluctuated at consistent uniform frequencies ω and 2 ω, then the only way fluctuating stars billions of light years away would be able to affect immediately the mass of the device here, would be through a superposition of advanced and retarded waves. But what is being fluctuated in CSUF experiments is the self-energy of the device here, **at the same location as the mass of the device,** rather than 10^8 light years away. What fluctuates is the device's self-energy – it is a **self-interaction effect**. Therefore there is no need for propagation of information faster than the speed of light.

Q5. Why doesn't the MEGA drive result in free energy, and therefore used for energy generation?

The MEGA drive does not violate energy conservation. The kinetic energy comes from the gravitational field, not from the electrical power applied to the device. There is a large nonzero gravitational potential in the universe we are tapping into to gain kinetic energy of the device. If we take a small amount of energy, practically no loss will be noticed by the whole universe. There are far more efficient ways of extracting energy, for example, from nuclear or solar power. Trying to extract energy from gravitation *via* the Mach effect is very inefficient.

The benefit of Mach effect propulsion is to avoid carrying propellant for long space missions, particularly for interstellar missions.

Q6. Does the MEGA drive violate General Relativity?

No the MEGA drive does not violate Einstein's general relativity.

The theory is based on Einstein's theory of gravitation. The mass change result can be obtained from general relativity.

The theory is Machian and fully consistent with Einstein's GR.

Q7. What natural systems might exhibit MEGA drive effects? Could these be observed, and how?

We have examined astronomical observations to see if they exhibited MEGA effects, which require two excitations (at frequencies f and 2f), but we haven't found anything yet. Such excitations do naturally occur in elliptical orbits (as one can ascertain from harmonic expansion). However, the naturally occurring frequencies (harmonics of the orbital periods) are not high enough to produce an observable effect. For example, the well-known binary pulsar PSR B1913+16 (also called the Hulse–Taylor binary after its discoverers) has an orbital period of 7.75 hours, and an eccentric orbit, resulting in totally unobservable orbital perturbations on the order of one part in 10^{30}.